# An analytical flow-by capacitive deionization model

Haverkort, J. W.; Sanderse, B.; Padding, J. T.; Blake, J. W.

**DOI**
10.1016/j.desal.2024.117408

**Publication date**
2024

**Document Version**
Final published version

**Published in**
Desalination

Desalination 582 (2024) 117408

Contents lists available at ScienceDirect

Desalination

journal homepage: www.elsevier.com/locate/desal

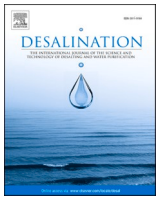

# An analytical flow-by capacitive deionization model

J.W. Haverkort [a,*], B. Sanderse [b], J.T. Padding [a], J.W. Blake [a]

[a] Delft University of Technology, Process & Energy Department, Leeghwaterstraat 39, 2628 CB Delft, the Netherlands
[b] Centrum Wiskunde & Informatica (CWI), Science Park 123, 1098 XG Amsterdam, the Netherlands

## HIGHLIGHTS

- A 2D transient flow-by capacity deionization model is studied computationally
- This comprehensive model is reduced to two coupled partial differential eqs.
- A fully analytical solution is obtained in terms of the Lambert W function
- Cell geometry and flow are optimized analytically for productivity and energy losses
- At the cost of high pressure drops the productivity can be increased tenfold

## GRAPHICAL ABSTRACT

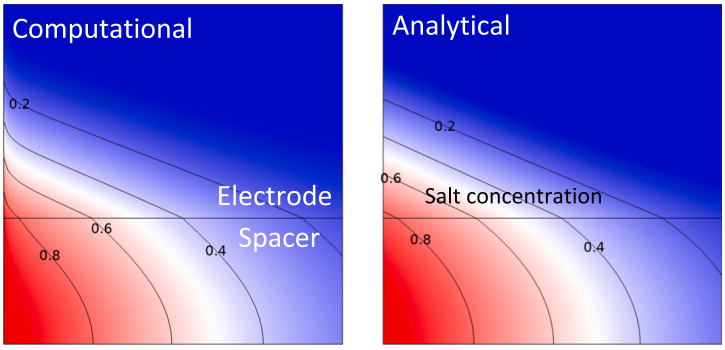


## ARTICLE INFO

*Keywords:*
Capacitive deionization
Transport modelling
Analytical solution
Design optimization

## ABSTRACT

In flow-by capacitive deionization (CDI) brackish water flows between two electrodes that capacitively remove salt. We assume low inlet concentrations so "salt shocks" appear in the electrodes and the process becomes diffusion-limited. For unit charge efficiency, a simplified model is derived consisting of two coupled partial differential equations. We obtain approximations, and exact solutions in terms of the Lambert W function, for the salt concentration as a function of time and space and for the equilibrium charge-voltage relation. These surprisingly simple solutions compare well with the results from comprehensive two-dimensional simulations. Useful analytical expressions are obtained for optimal geometrical and operational parameters that maximize the productivity and minimize the specific energy losses. By making cells much thinner the productivity can be increased an order of magnitude compared to typical values in the literature. The optimal electrode is found to be roughly six times thinner than the spacer. The associated pressure drop is around 0.4 bar per 1 mM of inlet salt concentration, making our recommendations practically feasible only for relatively low concentrations. The obtained model and analytical expressions provide useful guidance to strongly improve the design process.

## 1. Introduction

Desalination of water is becoming more economical and necessary in a number of isolated regions with scarce freshwater supply. Common methods include distillation, reverse osmosis, and various types of electrochemical deionization including reverse electrodialysis [1]. Advantages of electrochemical techniques include that part of the used energy can be recovered, and that at low concentrations it can be energetically more favourable to remove ions from the water, rather

* Corresponding author.
*E-mail address:* J.W.Haverkort@tudelft.nl (J.W. Haverkort).

https://doi.org/10.1016/j.desal.2024.117408
Received 12 February 2023; Received in revised form 11 January 2024; Accepted 2 February 2024
Available online 8 February 2024

**Nomenclature**

| | |
|---|---|
| $A$ | electrode area [m$^2$] |
| $c$ | salt concentration [mol/m$^3$] |
| $c_0$ | inlet salt concentration [mol/m$^3$] |
| $c$ | cup-mixing concentration $\frac{1}{UL_s}\int_{-L_s/2}^{L_s/2} ucdy$. [mol/m$^3$] |
| $C_m$ | volumetric capacitance [F/m$^3$] |
| $D$ | diffusivity in spacer [m$^2$/s] |
| $D_e$ | effective electrode diffusivity [m$^2$/s] |
| $j$ | ion flux magnitude $j(x)$ [mol/s/m$^2$] |
| $j_i$ | molar ion flux $j_i(y)$ [mol/s/m$^2$] |
| $k$ | between 1.4 and 1, see Eq. (A.2) |
| $L$ | channel length in $x$-direction [m] |
| $L_e$ | electrode thickness [m] |
| P | productivity $UL_s/L$ [m/s] |
| $q_m$ | half charge density $\frac{c_m^+ - c_m^-}{2}$ [mol/m$^3$] |
| $T$ | charging time [s] |
| $t$ | time [s] |
| $U$ | average channel velocity [m/s] |
| $u$ | channel velocity profile $u(y)$ [m/s] |
| $V_T$ | thermal potential $RT/F = k_BT/e$ [V] |
| $V_{ext}$ | externally applied cell voltage [V] |
| $w$ | counterion density minus $w_0$, Eq. (33) |
| $w_0$ | value at $t \sim t_{RC}$: $\bar{w}_0 = e^{\bar{\mu}_{att}}$, |
| $w_m$ | half the total ion density $\frac{c_m^+ + c_m^-}{2}$ [mol/m$^3$] |
| $x$ | streamwise coordinate [m] |
| $y$ | transverse coordinate from centre [m] |
| $z$ | ion charge number [−] |

*Constants*

| | |
|---|---|
| $F$ | Faraday's constant 96485.332… [C/mol] |
| $R$ | gas constant 8.31446… [J/mol/K] |

*Dimensionless numbers*

| | |
|---|---|
| $\bar{c}, \bar{w}, \bar{q}$ | molar densities divided by $c_0$ |
| $\bar{D}$ | diffusivity ratio $D/D_e$ |
| Gz | Graetz number $UL_s^2/LD$ |
| $p$ | porosity $p = p_m + p_M$ |
| $\bar{L}_s$ | spacer thickness divided by $L_e$ |
| $\bar{L}$ | channel length divided by $L_e$ |
| $Sh_s$ | spacer Sherwood number $\frac{j}{D(c-c_{se})}$ |
| $\tilde{Sh}$ | based on electrode properties $\frac{Sh_s DL_e}{2L_s D_e}$ |
| $\bar{t}$ | time divided by $t_D = L_e^2/D_e$ |
| $\tilde{t}$ | re-scaled time $\frac{c_0}{p_m w D_e}\left(\frac{Sh_s D}{2L_s}\right)^2 t$ |
| $\hat{t}$ | transformed time $\sqrt{1+2\tilde{t}} - 1$ |
| $\tilde{V}$ | defined by $\bar{V}_{ext}/2 + \bar{\mu}_{att} - \Delta\bar{\phi}_\Omega$ |
| $\bar{x}$ | streamwise coordinate $x/L$ |
| $\tilde{x}$ | re-scaled coordinate $\frac{DSh_s}{2UL_s^2}x$ |
| $\bar{y}$ | transverse coordinate $y/L$ |
| $\tilde{\delta}$ | concentration profile thickness $\sqrt{1+2\tilde{t}}$ |
| $\tilde{\zeta}$ | re-scaled shock location $\tilde{Sh}\zeta$ [m] |
| $\bar{\phi}, \bar{\mu}_{att}, \bar{V}_{ext}$ | potentials divided by $V_T$ |

*Greek variables*

| | |
|---|---|
| $\Delta p$ | pressure drop [s] |
| $\mu_{att}$ | attraction chemical potential [V] |
| $\phi$ | electrostatic potential [V] |
| $\zeta$ | dimensionless location $\frac{y-L_s/2}{L_s/2}$ of salt shock |

*Subscripts and other notation*

| | |
|---|---|
| $\Omega$ | ohmic |
| $W(x)$ | Lambert W function $W(x)e^{W(x)} = x$ |
| $i$ | ion index $i = +, -$ |
| c | charged fully ($\zeta = 1$) |
| D | Donnan |
| e | electrode |
| M | macropore |
| M | micropore |
| s | spacer |
| se | spacer-electrode interface |

than the water from the ions.

In Capacitive De-Ionization (CDI) [56], a voltage is applied to high surface-area porous electrodes, typically composed of activated carbon. During the adsorption or *charging* phase, positive ions (cations) are stored in the pores of the negative electrode (cathode) and negative ions (anions) in the positive electrode (anode). This electro-sorption process leads to a purified stream of desalinated water. Because more counter-ions (with opposite charge compared to that of the electrode) are absorbed than co-ions (with equally signed charge as the electrode) are expelled from the pores, the net effect is that ions are removed from the solution. During the desorption, flushing, or *discharging* phase the electrodes are typically short-circuited, so as to release the salt again before a new cycle can start. Part of the stored energy spent during the charging phase can be recovered during this discharging phase. The applied voltage is typically around but below 1.23 V, above which water splitting can occur. CDI is claimed to require less energy than incumbent technologies at low salt concentrations below a few g/l [66], a few times 20 mM, although these numbers have been questioned relatively recently [50]. Experimental results reported thus far show low thermodynamic energy efficiencies [58], but CDI is still a relatively immature technology, so strong improvements can still be made. Energy efficiencies similar to those in reverse osmosis should in principle be possible [58]. New electrode materials can lead to a small improvement, but the largest improvements may be expected to come from system design, including the reduction of resistive losses. Also, for low salinities the energy consumption is low so other factors like capital costs, scalability, operational ease and reliability become more important [46]. Strong advantages of CDI include its lack of membranes, which would add cost and fouling, its flexible operation, and the possibility to store and partially recover energy.

Capacitive deionization received a lot of attention from the academic community in the last two decades, but has a much longer history [43,49]. Initially referred to as 'electrochemical demineralization' its development was first reported in 1960 [14]. Continuous operation with a separate outlet for concentrate and freshwater streams was made possible through 'parametric pumping' [42] using synchronized valves and applied potentials. At the end of the century, 1000 kg/h demonstration 'flow through capacitors' (FTC) were designed [2] and several other case studies were developed [43]. Later, many larger commercial plants became operational [56].

Initially, Faradaic redox reactions and potential reversal were thought to be required. In 1970, the charging of the electric double layer (EDL) was correctly identified as the main mechanism responsible for charge sorption [30]. As a result, performance was improved using asymmetric half-cycle operation without polarity reversal. Various types of carbonaceous material [48] like porous activated carbon, carbon cloth, aerogels [18] and more recently carbon nanotubes, graphene, and biochar [15] are used for CDI, due to their high surface area, low cost,

reasonable conductivity, and chemical stability.

The majority of studies published up to relatively recently [57] concern the flow-by or flow-between configuration, consisting of two porous carbon electrodes placed between current collectors close to each other, separated by a channel or a spacer. Other traditional configurations include flow-through (with flow parallel to the current) [55], desalination with wires [49], or membrane CDI (MCDI, with ion exchange membranes on either side of the channel) [37]. Recent variations on the flow-by architecture receive increased attention, including inverted CDI (i-CDI: acid and amine-treated electrodes give adsorption during short-circuiting and salt release during charging), flow-electrode CDI (FCDI, MCDI with flowing electrodes) [53,61,62], the desalination battery (flow-by with Faradaic redox reactions to increase salt storage capacity), hybrid-CDI (HCDI, one battery and one capacitive electrode), and cation intercalation desalination (CID, two battery electrodes, and separate fresh and concentrated channels between an anion exchange membrane (AEM)) [57]. The resulting enhanced design flexibility helps to increase the storage capacity but also the selectivity, allowing preferential adsorption of specific ions [20,63].

The first mathematical cell model for CDI [37] concerned a one-dimensional simplification to two variables describing the concentrations inside the spacer and inside the electrode, both varying with the streamwise coordinate and time. The flux was assumed to be due to both potential and concentration differences between the spacer and electrode, with proportionality factors fitted to experimental data. An analytical series-solution was obtained that compared very well with experimental data. Nonetheless, this successful model seems to not have been used subsequently or further developed. Ref. [31] developed a one-dimensional model, neglecting diffusion, but including both electrolyte and electrode resistance. The electric double layer was modelled as a pure capacitor. An analytical solution for the Laplace transform of the current density was used to study the time-behaviour. A much simpler zero-dimensional model treats the spacer as an ideal continuous stirred tank reactor (CSTR) [12], an assumption also used in for example Refs. [3,24,26,29,38,51]. In e.g. Refs. [11,33,67] various CSTRs were placed in series to create a one-dimensional model that approaches plug flow reactor (PFR) behaviour. A 1D flow-though CDI model was developed in Ref. [22]. In Ref. [38] a quasi-two-dimensional numerical model was made by considering the two directions separately (1D + 1D), neglecting streamwise diffusion and electro-migration. Ref. [54] compares resolved 2D-pore scale simulation with homogenized continuum models and found only relatively small differences in integral parameters like stored salt. Local variables like salt concentration showed much larger differences, highlighting the need for accurately including tortuosity and other effective parameters. Finally, Ref. [50] describes a Randles electrical circuit, consisting of a parallel resistance and capacitance in series with a second resistance. While for some operating conditions reasonable fits can be made to experimental data, such simplified models are not useful for optimization of operating and geometrical parameters. They also cannot describe the salt shock regime we consider here [40].

Besides these cell models, the last fifteen years saw many theory papers focusing on improving the mathematical description of the double layer. Initially [6,8,12], the double layer was described by a thin Stern layer associated with the minimum distance that ions can approach the surface, in combination with a thicker diffuse layer described by the Gouy-Chapman model based on an analytical solution of the Poisson-Boltzmann equation. In this Gouy-Chapman-Stern (GCS) model a constant capacitance is added to a potential-dependent capacitance. It was soon realized that the smallest pores typically have electric double layers that strongly overlap, allowing the Donnan assumption of constant pore potential and counterion concentration to be used. In the developed modified Donnan (mD) model [9,13] a distinction between micropores (<2 nm) and macropores was made, somewhat similar to in Ref. [31], with a potential difference between them. This potential jump consists of the sum of the Donnan potential and a capacitive voltage, associated with a Stern layer but potentially also with quantum capacitance or space charge inside the solid [10,28]. The Donnan equilibrium in the micropores includes an attraction term $\mu_{att}$ that describes the chemical potential of adsorption in the absence of an applied field. Using a concentration-independent value for $\mu_{att}$ can strongly overpredict the non-electrostatically adsorbed salt at high concentrations. Therefore, the improved modified Donnan model (i-mD) [10] was developed to account for repulsive Coulombic interactions, resulting in an inverse proportionality between $\mu_{att}$ and the micropore ion concentration. The amphoteric Donnan model (amph-DM) [7,36] does not include the attraction term but instead considers regions of positive and negative fixed charged associated with charged surface-groups co-existing inside each electrode. To simplify the analysis while retaining a reasonable degree of generality and accuracy, in the present work we consider the mD model without these later improvements and assume a constant capacitance. Instead of further improving the double layer models, this work focuses on macroscopic transport modelling useful for cell and parameter optimization.

An important quantity that these models predict is the charge efficiency $\Lambda$ [4,31,64],[1] which gives the fraction of the total ionic charge that is used for desalting. At low voltages compared to the thermal voltage $V_T = RT/F$, co-ions inside the micropores are merely swapped with counter-ions from outside the micropores [59]: for each two electrons an ion is both expelled and adsorbed [10]. Since in the opposite electrode the same happens no net salt will be absorbed and $\Lambda = 0$. As the voltage is increased, co-ions are removed, increasing the capacitance. A further increase in voltage leads to counter-ion insertion and an increasing $\Lambda$ [59]. The charge efficiency has been found to depend only on the potential drop over the diffuse layer in a GCS model or the Donnan potential drop in a modified Donnan model.

The modified-Donnan model showed for the first time salt 'shock waves' consisting of sharp 'desalting fronts' moving into the porous electrodes. These can be seen in Fig. 9 of Ref. [9], reproduced in Fig. 16 of Ref [49], or in graphs associated with the 20 mM case of the supporting information of Ref. [27]. At high potentials, the macropores are virtually depleted of salt. When the micropores cannot adsorb more salt, the desalting front moves on. A similar salt depletion occurs in the GCS model, see e.g. Ref. [8] but here the macropore concentration does not vanish and the shock is more smooth. Similar 'deionization shocks' have been studied in [17,35], associated with salt depletion and associated concentration polarization in porous membranes. A first 2D CDI model was reported in Ref. [27] for a flow-by configuration using the modified-Donnan model, and implemented in the finite element solver COMSOL. These simulations showed salt depletion shocks moving through the electrode in both directions. A similar model was used in Ref. [52]. Various methods were reported to improve the numerical stability [40,41].

The analytical model derived in this work combines the transient diffusive transport towards a narrow propagating adsorption or reaction front with advective transport in the perpendicular direction. Given the generic nature of this configuration, it may also find usage in other fields [23], including, for example, phase-change thermal batteries [60], sorption systems for thermal energy [44], cross-flow filtration combustion [16], convection batteries [21], or electrochemical micro-reactors [19]. There are several ways in which our model may be extended, for example, by considering the discharging phase or recycling, different reaction- or adsorption kinetics, or different configurations including multiple channels and/or membranes, etc.

This paper continues in Section 2 with reviewing the computational two-dimensional, transient, dilute, symmetric, binary electrolyte equations of Ref. [27] in dimensionless form. Section 3 discusses the

[1] This is sometimes referred to as the electric double layer (EDL) charge efficiency $\lambda_{dl}$ [51]. The ionic current can be lower than the electronic current due to leakage currents, which is quantified by the Coulombic efficiency $\lambda_c$. The product of the two is called the *dynamic* charge efficiency.

assumptions required to derive a reduced model and derives accurate explicit analytical expressions for the equilibrium micropore salt concentration and Donnan potential. A reduced model is derived in Section 4, resulting in two dimensionless coupled partial differential equations (PDEs). We obtain useful very simple solutions to these equations in Section 5 for low and high dimensionless times. Section 6 shows that the solutions of our reduced model reasonably accurately describe the results of the full computational model. Finally, in Section 7 the analytical solutions are used to provide explicit expressions for optimal design parameters.

## 2. Full model

Fig. 1 shows the domain under consideration, its dimensions, the coordinate system used and typical profiles for the velocity $u(y)$, concentration $c(x,y,t)$ and the electrostatic potential in the electrolyte $\phi(x,y,t)$.

### 2.1. Assumptions

Our model equations and notation will mostly follow that of Ref. [27], which assumes:

- A dilute, quasi-neutral, binary electrolyte with constant and equal effective diffusivity $D_e$ for both ions.
- A constant attraction potential $\mu_{att}$ within the modified Donnan (mD) model, accounting for non-electrostatic adsorption, equal for both ions,
- Biporous electrodes with constant macropore porosity $p_M$, micropore porosity $p_m$, total porosity $p = p_m + p_M$, a constant electronic potential, and constant capacitance per unit micropore volume $C_m$.

In the mD model the micropore concentration $c_{m,i}$ of ion species $i$ with valency $z_i$ is related to the local macropore concentration $c_{M,i}$ by a Boltzmann distribution

$$c_{m,i} = c_{M,i} e^{-z_i \Delta\bar{\phi}_D + \bar{\mu}_{att}}, \tag{1}$$

where the dimensionless Donnan potential $\Delta\bar{\phi}_D = \Delta\phi_D/V_T$ and dimensionless non-electrostatic attraction potential $\bar{\mu}_{att} = \mu_{att}/V_T$ are both non-dimensionalized with the thermal potential $V_T = \frac{RT}{F} \approx 25$ mV. As illustrated in Fig. 2, in the positive electrode the Donnan potential drop $\Delta\phi_D$ is positive so that the micropore concentration of cations with positive $z_i$ will be lower, and the anion micropore concentration will be higher than the macropore concentration. In the negative electrode the opposite will happen. See also Fig. 3.

The Donnan potential is the difference in potential between the micropores and the macropores. The micropore potential drop is related to the micropore charge density $2q_m$ by

$$\Delta\phi_m = -2F\frac{q_m}{C_m}. \tag{2}$$

This represents the potential drop between the solid bulk and the diffuse layer of the micropore. This includes a drop over the Stern layer, but potentially also inside the solid [10,28]. It is modelled as a capacitor with effective volumetric capacitance $C_m$ [F/m$^3$] and charge density $2q_m$ [mol/m$^3$], both per unit *micropore* volume. From Eq. (1) we find

$$2q_m \equiv c_m^+ - c_m^- = -2ce^{\bar{\mu}_{att}} \sinh\Delta\bar{\phi}_D, \tag{3}$$

where we use electroneutrality in the macropores to give $c_{M,+} = c_{M,-} = c$. Similarly the ion concentration reads, using Eq. (1)

$$2w_m \equiv c_m^+ + c_m^- = 2ce^{\bar{\mu}_{att}} \cosh\Delta\bar{\phi}_D. \tag{4}$$

The Donnan and micropore potential together make up the difference between the potential in the electrode and the electrolyte in the macropore, see also Figs. 2 and 3:

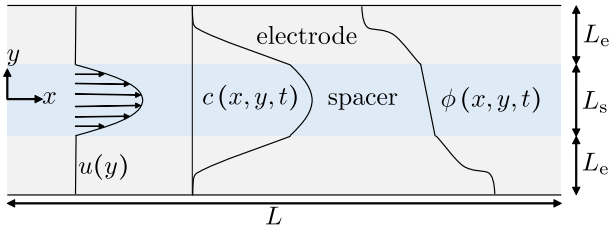


**Fig. 1.** A schematic introducing the geometry, coordinates, and concentration $c$ and potential $\phi$ profiles in the flow-by capacitive deionization set-up under consideration, based on Ref. [27].

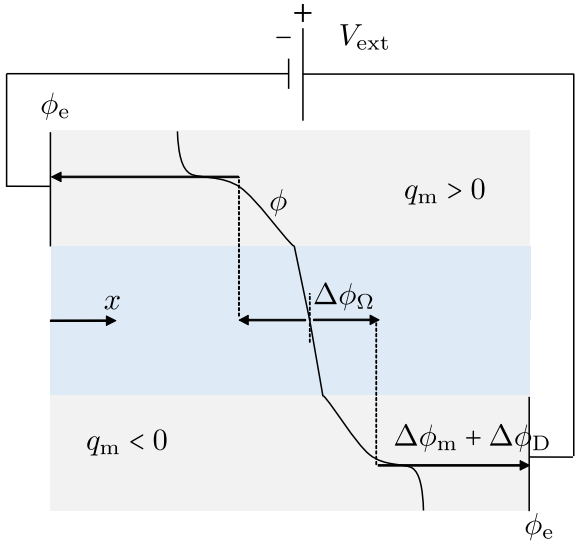


**Fig. 2.** The potential $\phi$ in the electrolyte, $\phi_e$ in the solid electrode, the drop $\Delta\phi_m$ in the micropores, the Donnan potential $\Delta\phi_D$ between the micro- and macropores, and the ohmic drop $\Delta\phi_\Omega$ between the centre of the channel and the location of the desalting front. This schematic shows how in the positive electrode the difference $\phi_e - \phi = \Delta\phi_m + \Delta\phi_D$ is positive, corresponding to a negative counterion charge. In the negative electrode this is negative and the counterion charge is positive. The applied potential $V_{ext} = 2(\Delta\phi_m + \Delta\phi_D + \Delta\phi_\Omega)$. Note that the electronic potential $\phi_e$ is constant throughout the electrodes so that the connection points may be anywhere. The sign of the micropore charge density $q_m$ is indicated.

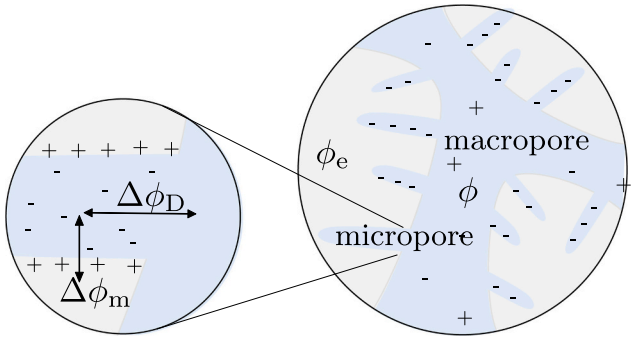


**Fig. 3.** An illustration of the charge distribution in the electroneutral macropores and the micropores of the positive electrode, in which negatively charged counterions concentrated near the electrode surface primarily in the micropores. A Donnan potential drop $\Delta\phi_D$ exists between the electrolyte potential $\phi$ in the macropores and that in the micropores. A further capacitive potential drop $\Delta\phi_m$ exists between the bulk solid and micropore electrolyte.

$$\phi_e - \phi = \Delta\phi_D + \Delta\phi_m. \tag{5}$$

*In the positive electrode* we have $\phi_e - \phi = V_{ext}/2 - \Delta\phi_\Omega$, see Fig. 2. Using this in Eq. (5) gives

$$\frac{V_{ext}}{2} = \Delta\phi_D + \Delta\phi_m + \Delta\phi_\Omega. \tag{6}$$

In the negative electrode, the potential drops on the right-hand side are all negative, so the left-hand side requires a negative sign. This potential balance does not explicitly include a finite potential of zero charge [5,51], but this can be easily included as a correction to the externally applied potential $V_{ext}$.

### 2.2. Dimensionless equations

In Ref. [27] the following dimensionless equations for the concentration and potential inside the porous electrodes are derived

$$\frac{\partial \bar{c}}{\partial \bar{t}} = \bar{\nabla}^2\bar{c} - \frac{p_m}{p_M}\frac{\partial \bar{w}_m}{\partial \bar{t}}, \tag{7}$$

$$\bar{\nabla}\cdot(\bar{c}\bar{\nabla}\bar{\phi}) = \frac{p_m}{p_M}\frac{\partial \bar{q}_m}{\partial \bar{t}}, \tag{8}$$

and inside the spacer region:

$$\frac{\partial \bar{c}}{\partial \bar{t}} + \frac{\bar{D}\mathrm{Gz}}{\bar{L}_s^2}\bar{u}\frac{\partial \bar{c}}{\partial \bar{x}} = \bar{D}\bar{\nabla}^2\bar{c}, \tag{9}$$

$$\bar{\nabla}\cdot(\bar{c}\bar{\nabla}\bar{\phi}) = 0. \tag{10}$$

Here, the dimensionless variables read[2]

$$\bar{t} = \frac{tD_e}{L_e^2},\ \ \bar{x} = \frac{x}{L},\ \ \bar{y} = \frac{y}{L_e},\ \ \bar{\nabla} = L_e\nabla,\ \ \bar{u} = \frac{u}{U}, \tag{11}$$

with $U$ the average flow velocity, $\bar{\phi} = \phi/V_T$, $\bar{c} = c/c_0$, $\bar{q}_m = q_m/c_0$, and $\bar{w}_m = w_m/c_0$, and dimensionless numbers

$$\bar{L}_s = \frac{L_s}{L_e},\ \ \bar{D} = \frac{D}{D_e},\ \ \mathrm{Gz} = \frac{UL_s^2}{LD},\ \ \bar{C}_m = \frac{V_T C_m}{2Fc_0}. \tag{12}$$

here $D_e$ is the effective medium diffusivity inside the porous electrode. Ref. [27] assumed $\bar{D} = 2$ as an approximate and reasonable estimate for electrodes of porosities between 0.6 and 0.8. The Graetz number Gz characterizes the ratio of advection and transverse diffusion in the spacer and $\bar{D}/\bar{L}_s^2$ corrects this for the chosen non-dimensionalization based on the effective diffusivity in the electrode and its thickness. The dimensionless micropore capacitance $\bar{C}_m$ can be used to write Eq. (2) as[3]

$$\Delta\bar{\phi}_m = -\frac{\bar{q}_m}{\bar{C}_m}. \tag{13}$$

With Eq. (3) we can then write Eq. (6) as

$$\frac{\bar{V}_{ext}}{2} = \Delta\bar{\phi}_D + \frac{\bar{c}}{\bar{C}_m}e^{\bar{\mu}_{att}}\sinh\Delta\bar{\phi}_D + \Delta\bar{\phi}_\Omega. \tag{14}$$

here we take $\bar{V}_{ext}/2 = \pm V_{ext}/2V_T$ to be positive on the positive electrode and negative on the negative electrode.

### 2.3. Time-scales

From a dilute binary electrolyte with equal effective diffusivity $D_e$ for both ions, the effective conductivity in the electrode associated with the inlet concentration $c_0$ reads

$$\kappa_{e,0} = \frac{2F^2D_e}{RT}c_0. \tag{15}$$

A characteristic resistance associated with the electrode is $L_e/\kappa_{e,0}A$ with $A$ the electrode area. The electrode capacitance per unit electrode volume is $p_mC_m$, so that multiplying with $AL_e$ gives the total electrode capacitance. Multiplying with the characteristic electrode resistance gives an *RC*-time,[4] related to the other two time-scales as follows

$$t_{RC} \equiv p_m\frac{L_e^2C_m}{\kappa_{e,0}} = p_m\bar{C}_m t_D, \tag{16}$$

$$t_D \equiv \frac{L_e^2}{D_e} = \frac{\bar{D}\mathrm{Gz}}{\bar{L}_s^2}t_U, \tag{17}$$

$$t_U \equiv \frac{L}{U}. \tag{18}$$

here $t_D$ is the characteristic diffusion time associated with the electrode thickness and $t_U$ the transit time of a fluid parcel with the average velocity $U$. For the parameters in Table 1, used in Ref. [27], these time-scales all have a similar magnitude of a few minutes.

**Table 1**
Dimensionless parameters used for the simulations in this work and Ref. [27]. Dimensional values leading to these values are e.g. $L_e = 0.68$ mm, $L_s = 0.8$ mm, $L = 100$ mm, $U = 0.438$ mm/s, $D = 1.9{\cdot}10^{-9}$ m$^2$/s, $D_e = 0.95{\cdot}10^{-9}$ m$^2$/s, $C_m = 1.5{\cdot}10^8$ F/m$^3$, $c_0 = 20$ mM, $\mu_{att} = 37.5$ mV, with $V_T = RT/F \approx 25$ mV, so $t_D = 487$ s, $t_U = 228$ s, and $t_{RC} = 365$ s. For the calculations we additionally use a dynamic viscosity $\mu = 1$ mPas.

| Symbol | Description | Value |
|---|---|---|
| $\bar{\mu}_{att}$ | Non-electrostatic adsorption parameter | 1.5 |
| $\bar{C}_m$ | Micropore capacitance | 0.97 |
| $p_m$ | Micropore porosity | 0.3 |
| $p_M$ | Macropore porosity | 0.4 |
| $\bar{L}_s$ | Length ratio $L_s/L_e$ | 1.18 |
| $\bar{L}$ | Length ratio $L/L_e$ | 147 |
| $\bar{D}$ | Diffusivity ratio $D/D_e$ | 2 |
| Gz | Graetz number $UL_s^2/LD$ | 1.48 |
| $\mathrm{Sh}_s$ | Spacer Sherwood number $\frac{jL_s/D}{c-c_{Se}}$ | 8.2 |
| $\bar{\mathrm{Sh}}$ | Spacer Sherwood number $\frac{\mathrm{Sh}_sDL_e}{2L_sD_e}$ | 7 |

## 3. Simplified model assumptions

To obtain approximate analytical solutions, in the next section we will derive a simplified mathematical model from the full equations discussed in the previous section. Here we will discuss the assumptions under which the required simplifications are valid. We will also derive new explicit analytical expressions for the micropore ion density and Donnan potential.

### 3.1. Time and length-scales

In the initial 'flushing' phase between $0 < t \leq t_U$ most of the fluid that leaves the channel has not traversed the full channel length. The charging time $T$ is the duration of the adsorption phase of the desalination cycle. We will assume $T \gg t_U$, to ensure that the flushing phase

[2] Note that while we use $L$ to non-dimensionalize $\bar{x} = x/L$, we use $L_e$ in the dimensionless nabla-operator $\bar{\nabla} = L_e\nabla$ for both the $x$ and $y$-component.

[3] Correcting a typo, an erroneous factor 2$F$, in Eq. (13) of Ref. [27].

[4] A similar expression, with $Dp_M/\tau^2$ instead of $D_e$, was called the electro-diffusion time constant in Ref. [52]. Here $\tau$ is the electrode tortuosity and the square seems to have been a typo.

makes up only a small fraction of the cycle. When $UL_e^2/DL \lesssim 1$ and $p_m \bar{C}_m \frac{UL_e^2}{DL} \lesssim 1$ this automatically implies that also $T \gg t_D, t_{RC}$ which are two further requirements for our analysis to hold. Our model will thus not include the initial dynamics and only consider times

$$t \gtrsim t_D, t_{RC}, t_U. \tag{19}$$

We will assume that the flow and concentration profiles are both fully developed[5] which will hold for

$$x \gtrsim 0.05 \frac{UL_s^2}{D} \gg 0.05 L_s. \tag{20}$$

### 3.2. Charge efficiency

We will consider here *the positive electrode*, for which $\Delta\bar{\phi}_D > 0$, but by (anti-)symmetry the same results will hold for the negative electrode upon changing the signs of $\Delta\bar{\phi}_D$, $\Delta\bar{\phi}_m$ and $\Delta\bar{\phi}_\Omega$. The differential charge efficiency, the fraction of ionic current density which contributes towards salt removal,[6] is given by:

$$\lambda \equiv -\frac{dw_m}{dq_m} = \tanh\Delta\bar{\phi}_D. \tag{21}$$

An important assumption we will make for the simplified model to hold is that $\lambda \approx 1$, which requires

$$\Delta\bar{\phi}_D \gtrsim 2. \tag{22}$$

In this limit, in the positive electrode Eqs. (3) and (4) give $2w_m \approx -2q_m \approx c_m^-$ so that in the micropores there are many more counter-ions than co-ions ($c_m^- \gg c_m^+$).[7] Or, dimensionless:

$$2\bar{w}_m \approx -2\bar{q}_m \approx \bar{c}e^{\bar{\mu}_{att}+\Delta\bar{\phi}_D}. \tag{24}$$

Defining

$$\frac{\tilde{V}}{2} \equiv \frac{\bar{V}_{ext}}{2} + \bar{\mu}_{att} - \Delta\bar{\phi}_\Omega, \tag{25}$$

and assuming Eq. (22) holds, we can solve Eq. (14) analytically to give[8]

$$\Delta\bar{\phi}_m = \frac{\bar{w}_m}{\bar{C}_m} = W\left(\frac{\bar{c}e^{\tilde{V}/2}}{2\bar{C}_m}\right). \tag{26}$$

here the Lambert W function is defined by

$$W(x)e^{W(x)} = x. \tag{27}$$

This function can be relatively easily evaluated numerically solving Eq. (27). However, we also note the following approximations developed in Appendix A

$$W\left(\frac{\bar{c}e^{\tilde{V}/2}}{2\bar{C}_m}\right) \approx \frac{\frac{\tilde{V}}{2} + \ln\left(\frac{\bar{c}}{2\bar{C}_m}\right)}{k} \approx \frac{\tilde{V}}{2} - \ln\left(\frac{2\bar{C}_m}{\bar{c}}\left[\frac{\tilde{V}}{2} + \ln\left(\frac{\bar{c}}{2\bar{C}_m}\right)\right]\right). \tag{28}$$

These approximations both have a relative error $\lesssim 15$ % for arguments $x \gg 1$ using $k \approx 1.15$.[9] This allows us to quantify Eq. (22). Eqs. (6) and (25) give $\Delta\bar{\phi}_D = \tilde{V}/2 - \Delta\bar{\phi}_m - \bar{\mu}_{att}$. Inserting Eq. (26) for $\Delta\bar{\phi}_m$ and using the second approximation of Eq. (28) allows $\Delta\bar{\phi}_D \gtrsim 2$ to be written as

$$\tilde{V} + 2\ln\left(\frac{\bar{c}}{2\bar{C}_m}\right) \gg \frac{\bar{c}e^{\bar{\mu}_{att}}}{\bar{C}_m}. \tag{29}$$

Using the numbers in Table 1 with $\bar{c} = 1$ gives a right-hand side of 4.5. The second term on the left-hand-side is about $-1.4$, so that Eq. (29) requires $\tilde{V} \gg 4.5$. This shows that only at high applied potentials around or above 1 V we can expect unit charge efficiency. It will be easier to satisfy this criterion at higher $\bar{C}_m$ or lower $\bar{\mu}_{att}$.

### 3.3. Initial concentrations

At $t < 0$, before a potential is applied, so $\Delta\phi_D = 0$, Eq. (1) gives the increased micropore concentration due to non-electrostatic adsorption as $\bar{c}_m^{\pm}(t = 0) = \bar{w}_0$, where

$$\bar{w}_0 = e^{\bar{\mu}_{att}}, \tag{30}$$

Fig. 4(d) shows the micropore concentration for various times, obtained from solving the full model of Section 2 using the parameters in Table 1 similar to the 20 mM simulations of Ref. [27].

For our simplified model we will assume that all co-ions are expelled from the micropores upon application of a cell potential. These expelled co-ions migrate towards the opposite electrode, where they add tp the micropore concentration of Eq. (30). This can be clearly seen from Fig. 4 (d) where the micropore concentration can be seen to double during roughly the *RC*-time deep in the electrode from $\bar{c}_m^{\pm}(t = 0) = e^{\bar{\mu}_{att}} \approx 4.5$ to $\bar{c}_m^{\pm}(t \sim t_{RC}) = 2e^{\bar{\mu}_{att}} \approx 9$.[10] Since in effect this process merely swaps the co-ions with an equal number of counter-ions the ion density $2w$ remains

[5] Since the liquid kinematic viscosity $\nu \gg D$, the hydrodynamic entrance length will be much shorter than the concentration entrance length. When the latter can be assumed small, an inlet section like that used in Ref. [27] will not be needed to obtain fully developed flow in the beginning of the channel. Eq. (20) follows from replacing in the thermal entrance length [32] the thermal diffusivity with the diffusivity. We can also argue for the validity of Eq. (20) heuristically. Using the Lévêque approximation, the boundary layer in a fully developed flow has a 99 % boundary layer thickness of $\delta_{99\%} = 1.607\left(\frac{L_s D x}{U}\right)^{1/3}$ so that inserting $x$ from Eq. (20) gives $\delta_{99\%} \gtrsim 0.6 L_s$. This shows that at this position the boundary layers from both sides will have started to overlap, a requirement for fully-developedness.

[6] This expression follows after using Eqs. (3) and (4). The charge efficiency reads $\Lambda = -\frac{w_m - w_0}{q_m}$, with $2w_0$ the micropore ion density at zero applied potential, so that $2w_m - 2w_0$ is the removed salt concentration. Inserting Eqs. (3) and (4) and using trigonometric relations this gives $\Lambda = \frac{\cosh\Delta\phi_D - 1}{\sinh\Delta\phi_D} = \tanh\frac{\Delta\phi_D}{2}$ as derived in Refs. [13,48]. Note that these expressions are similar but slightly different from those in a GCS model. Ref. [6] found $\Lambda = \tanh(\Delta\phi_d/4)$ and Ref. [12] obtained a differential charge efficiency $\lambda = \tanh(\Delta\phi_d/2)$, with $\Delta\phi_d$ the diffuse layer potential drop.

[7] With this assumption Eqs. (7) and (8) can be combined to give

$$\frac{\partial\bar{c}}{\partial\bar{t}} = \bar{\nabla}^2\bar{c} + \bar{\nabla}\cdot(\bar{c}\bar{\nabla}\bar{\phi}). \tag{23}$$

Neglecting the time-dependence of $\phi_e$ and $\Delta\phi_D$, Eqs. (5), (8), and (13) give $\frac{\partial\bar{\phi}}{\partial\bar{t}} = -\frac{\partial\Delta\bar{\phi}_m}{\partial\bar{t}} = \frac{1}{\bar{C}_m}\frac{\partial\bar{q}_m}{\partial\bar{t}} = \frac{p_M}{p_m\bar{C}_m}\bar{\nabla}\cdot(\bar{c}\bar{\nabla}\bar{\phi})$. This is a diffusion equation for the potential with a dimensionless diffusion coefficient given by $\frac{p_M\bar{c}}{p_m\bar{C}_m} = p_M\frac{t_D}{t_{RC}}\bar{c}$. *Re*-inserting dimensions gives a diffusivity $p_M L_e^2\bar{c}/t_{RC} = \frac{\kappa_e}{p_m C_m/p_M}$, with $\kappa_e$ the ionic conductivity similar to Eq. (15) and $p_m C_m/p_M$ the capacitance per unit macropore volume.

[8] With Eq. (22) we have $\sinh\Delta\bar{\phi}_D \approx e^{\Delta\bar{\phi}_D}/2$. Equation (14) can be written as $\tilde{V}/2 = x + \frac{\bar{c}}{2\bar{C}_m}e^x$, where $x = \Delta\bar{\phi}_D + \bar{\mu}_{att}$. With Eq. (27), this equation is solved by $x = \tilde{V}/2 - W\left(\frac{\bar{c}e^{\tilde{V}/2}}{2\bar{C}_m}\right)$ so that for $\Delta\bar{\phi}_m = \frac{\bar{c}e^x}{2\bar{C}_m}$ we obtain Eq. (26). We note a formal analogy with the quasi-Fermi level model in Ref. [68] where electrons and holes are analogous to our anions and cations.

[9] Depending on the specific parameters used $1 < k < 1.3$, see Eq. (A.2). Using the variables in Table 1 for $\bar{V}_{ext} = 40$, Eq. (A.2) gives $k \approx 1.15$. The relative error of the second approximation in Eq. (28) rapidly decreases to zero for large arguments $x$.

[10] We note that $t_{RC}$ is an e-folding time-scale so that $t \sim t_{RC}$ should be taken to mean at a time several times $t_{RC}$ such that the potential profile has fully developed.

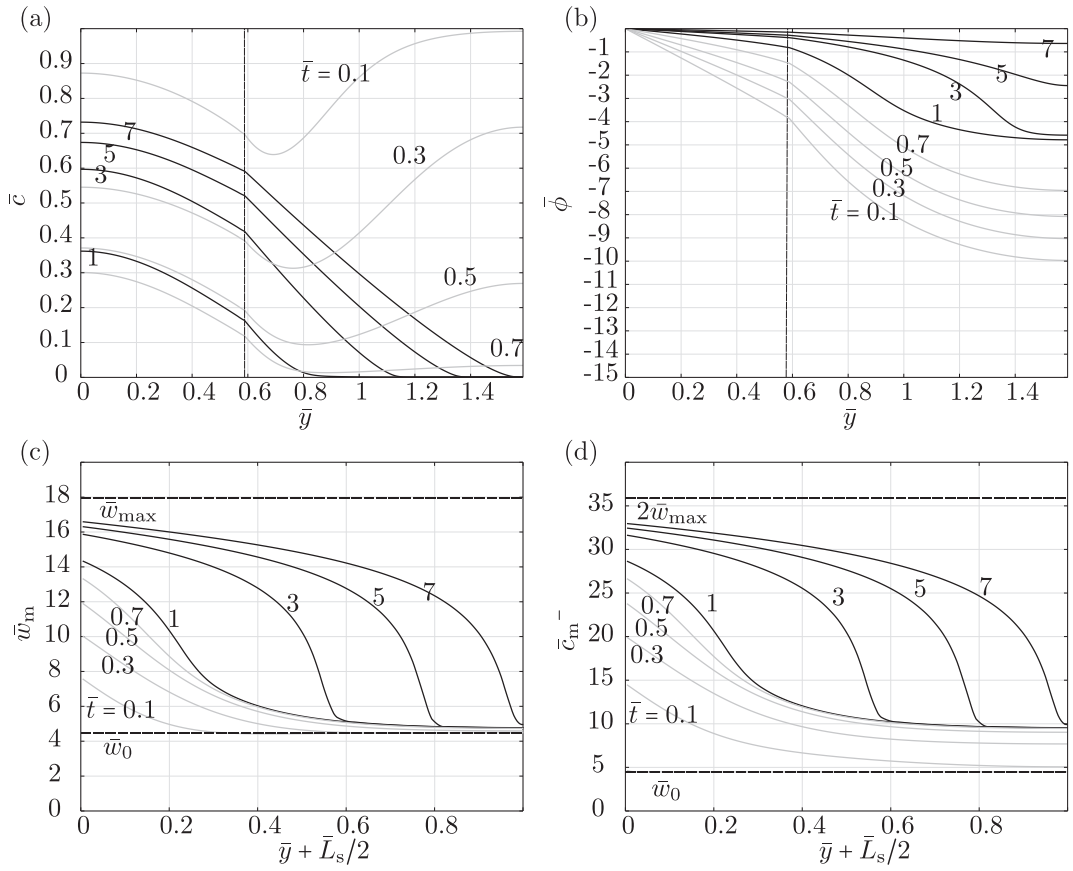


**Fig. 4.** Simulation results halfway the channel at $x = L/2$ for $\bar{V} \approx 40$ of (a) the macropore concentration $\bar{c}$; (b) the electrolyte potential $\bar{\phi}$; (c) the half-ion concentration $\bar{w}_{\rm m}$ and (d) the counterion micropore concentration, compared to $\bar{w}_0$ from Eq. (30) and $\bar{w}_{\rm max}$ from Eq. (32). Using $\bar{\mu}_{\rm att} = 1.5$ from Table 1 gives $\bar{c}_{\rm m}^{\pm}(t = 0) \approx 4.5$. This value can be seen for the $t = 0$ curve in Fig. 4(d). Once applied, the potential diffuses through the porous electrode over a time-scale $t_{RC}$ given by Eq. (16). With the parameters in Table 1 Eq. (16) gives $\bar{t}_{RC} = p_{\rm m}\bar{C}_{\rm m} = 0.3$. Over roughly this time-scale the potential can be seen to develop in Fig. 4(b) into a quasi-stationary profile coupled to the much slower evolution of the concentration profile. After $\bar{t} \approx 1$ the shock is fully formed and the concentration approximately vanishes after some depth into the electrode.

unaltered, as seen from Fig. 4(c).

For the chosen potential of $\bar{V} = 40$, Fig. 4(a) shows that deep into the electrode the macropore concentration approximately vanishes. This negligible macropore concentration will be an important assumption in our simplified model.[11] Therefore, we investigate under which conditions this will happen. In Appendix A we derive an expression, Eq. (A.7), for the dimensionless macropore concentration. With $\bar{w}_{\rm m} = \bar{w}_0$, the macropore concentration will be small when

$$\bar{c}(\bar{t} \sim \bar{t}_{RC}) \approx 2\bar{C}_{\rm m} e^{\frac{k w_0}{\bar{C}_{\rm m}} - \frac{\bar{V}}{2}} \ll 1. \tag{31}$$

With the parameters of Table 1 and $k \approx 1.3$ this requires $\bar{V}_{\rm ext} \gtrsim 15 + 2\Delta\bar{\phi}_\Omega$, or about 0.4 V neglecting the ohmic drop. Eq. (31) is also plotted in Fig. 5.

Eq. (31) is a requirement of the developed analytical model, and therefore poses a restriction to what parameters can be used. For typical porosities and potentials it will usually require $\bar{C}_{\rm m} = \frac{V_T C_{\rm m}}{2Fc_0} \gtrsim 1$. So the electrode capacitance has to be sufficiently large to accommodate the inlet salt concentration $c_0$. Unless much higher capacitance electrodes ($C_{\rm m} \gg 10^8$ F/m$^3$) are developed, this will typically limit application of our model to relatively low concentrations $c_0 \ll 0.1$ M.

### 3.4. Salt adsorption capacity

The highest salt concentration in the micropores is obtained under equilibrium conditions when $\bar{c} = 1$ and there is no current so $\Delta\bar{\phi}_\Omega = 0$. In this case Eq. (26) gives $\bar{w} = \bar{w}_{\rm max}$

$$\bar{w}_{\rm max} \approx \bar{C}_{\rm m} {\rm W}\left(\frac{e^{\bar{V}_{\rm ext}/2 + \bar{\mu}_{\rm att}}}{2\bar{C}_{\rm m}}\right) \approx 0.87\bar{C}_{\rm m}\left[\frac{\bar{V}_{\rm ext}}{2} + \bar{\mu}_{\rm att} - \ln(2\bar{C}_{\rm m})\right], \tag{32}$$

where we used the first approximation of Eq. (28) with $k \approx 1.15$. The Lambert W function can also be easily evaluated numerically, solving Eq. (27). Using the variables in Table 1, Eq. (32) gives $\bar{w}_{\rm max} \approx 18$ or $2\bar{w}_{\rm max} \approx 36$, very close to the equilibrium concentration for $\bar{t} = 1$ in Fig. 4(a) and also in Ref. [27] and its supporting information.

Of this maximum counter-ion density 'adsorption capacity', only a

[11] The observant reader may wonder where this macropore concentration goes as it does not seem to add much to the micropore concentration deep inside the electrode. Actually, it does go into the micropores but it primarily diffuses to near the spacer where the available potential is highest. This can be clearly seen from the macropore concentration profiles for small times. It is verified by the observation that after the *RC*-time the micropore concentration deep in the electrode has not increased much above $2w_0$.

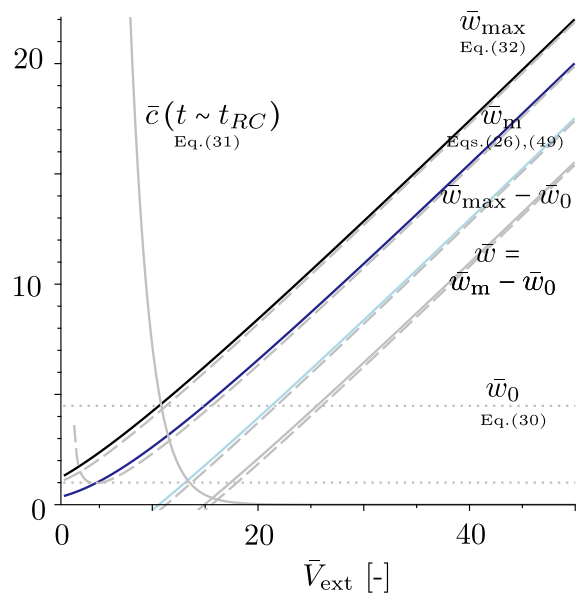


**Fig. 5.** Various measures for the dimensionless micropore capacity $\bar{w}_{\mathrm{m}}$ and that initially taken up by ions from the macropores and expelled from the counter-electrode $\bar{w}_0$ as a function of the dimensionless cell potential $\bar{V}_{\mathrm{ext}} = \frac{F}{RT}V_{\mathrm{ext}}$. The maximum capacity $\bar{w}_{\max}$ is only reached upon equilibrium. Including the effect of ohmic losses and a decreased macropore concentration, the remaining capacity is $\bar{w}_{\mathrm{m}}$. In applying the indicated equations we used the parameters in Table 1 along with $\bar{c} = 0.5$, and Eq. (49) with $\zeta = 0.5$ to evaluate the ohmic drop. The solid lines use the exact solution, while the dashed lines indicate the approximation of Eq. (26) which can be seen to strongly deviate only for low voltages, which give small arguments $x$ in $W(x)$. Validity of the analytical solutions derived in this work require $\bar{c}(t \sim t_{RC}) \ll 1$, which can be seen to be the case for $\bar{V}_{\mathrm{ext}} \gtrsim 18$ or $V_{\mathrm{ext}} \gtrsim 0.45$.

part can be used for adsorption of ions from the channel. After the *RC*-time $t_{RC}$ part of it is taken up by $\bar{w}_0$ given by Eq. (30). We will denote the remaining amount[12] with $\bar{w}_{\mathrm{m}} - \bar{w}_0$, which with Eq. (26) reads

$$\bar{w} = \bar{C}_{\mathrm{m}} \mathrm{W}\left(\frac{\mathrm{e}^{\bar{V}/2}}{2\bar{C}_{\mathrm{m}}}\right) - \mathrm{e}^{\bar{\mu}_{\mathrm{att}}}. \tag{33}$$

For the numbers in Table 1, neglecting $\bar{\phi}_\Omega$, and with $\bar{V}_{\mathrm{ext}} = 40$, Eq. (33) gives $\bar{w} \approx 18.5 - 4.5 = 13$, see Fig. 5. As a final criterion for our simplified model we require that the amount of salt that can be maximally stored in the two electrodes is substantially larger than that which is initially present in the spacer. This will allow focussing on desalination over time-scales $t \gtrsim t_U$ as indicated by Eq. (19). This can be quantified by $4w_{\max}p_{\mathrm{m}}AL_{\mathrm{c}} \gg c_0 AL_{\mathrm{s}}$ or, roughly

$$\bar{w} \gg \frac{\bar{L}_{\mathrm{s}}}{p_{\mathrm{m}}}. \tag{34}$$

[12] Part of it will also be taken up by the ions in the macropores. These ions will however preferentially adsorb near the channel-side of the porous electrode, where the available potential is highest. Therefore, we prefer to take this into account as an initial condition to our simplified model. The actual adsorption capacity will vary along the channel as the local macropore concentration decreases and the ohmic drop changes. Not taking this spatial and temporal variation into account constitutes on of the major simplifications in our analytical model. In Eq. (49) we find that the ohmic drop in the channel is approximately constant and that in the electrode can often be neglected so that $\bar{\phi}_\Omega \approx 1$. Therefore, we could take the ohmic drop into account in an approximate manner using a constant $\bar{V} = \bar{V}_{\mathrm{ext}} + \bar{\mu}_{\mathrm{att}} - 1$.

For the numbers in Table 1, $\bar{L}_{\mathrm{s}}/4p_{\mathrm{m}} \approx 1$, so that for medium to high voltage this criterion will be satisfied.

## 4. Simplified model derivation

In this section we will use the assumptions discussed in the previous section to derive from the full model equations of Section 2.2 a simplified mathematical model. This model will be approximately valid on time-scales larger than the *RC*-time $t_{RC}$, diffusive time $t_D$, and transit time $t_U$ viz. Eq. (19). The applied potential $\bar{V}_{\mathrm{ext}}$ has to be sufficiently large to ensure a unit charge efficiency viz. Eq. (29) and negligible macropore concentration viz. Eq. (31), especially at the higher dimensionless capacitances $\bar{C}_{\mathrm{m}}$ required by Eq. (34).

### 4.1. Spacer

The second inequality of Eq. (20), $UL_{\mathrm{s}}/D \gg 1$, allows us to neglect axial diffusion relative to advection ($D\partial^2/\partial x^2 \ll u\partial/\partial x$). The restriction to time-scales $t \gg t_U$ of Eq. (19) allows neglecting the time-dependence of the concentration profile relative the advection term ($\partial/\partial t \ll u\partial/\partial x$). Therefore, Eq. (10) can be approximated by

$$u\frac{\partial c}{\partial x} = D\frac{\partial^2 c}{\partial y^2}. \tag{35}$$

The salt flux $j$ [mol/s/m$^2$] leaving the channel through each side

$$j = -D\frac{\partial c}{\partial y}\bigg|_{L_{\mathrm{s}}/2} = D\frac{\partial c}{\partial y}\bigg|_{-L_{\mathrm{s}}/2}. \tag{36}$$

During charging $j \geq 0$. Integrating Eq. (35) from $y = -L_{\mathrm{s}}/2$ to $L_{\mathrm{s}}/2$ using the boundary conditions (36) gives

$$UL_{\mathrm{s}}\frac{dc}{dx} = -2j. \tag{37}$$

where the cup-mixing average concentration (note the relatively small difference in typography between $c$ and $c$) is defined as

$$c \equiv \frac{1}{UL_{\mathrm{s}}}\int_{-L_{\mathrm{s}}/2}^{L_{\mathrm{s}}/2} ucdy. \tag{38}$$

A factor $-2$ appears in Eq. (37) since $j$ is the positive flux entering one electrode, while what we need here is the flux leaving the channel through both sides. For a fully-developed concentration profile, the dimensionless Sherwood number, characterizing the total convective mass transfer relative to purely diffusive mass transfer [39], reads

$$\mathrm{Sh}_{\mathrm{s}} \equiv L_{\mathrm{s}}\frac{\frac{\partial c}{\partial y}\big|_{-L_{\mathrm{s}}/2} - \frac{\partial c}{\partial y}\big|_{L_{\mathrm{s}}/2}}{c - c_{\mathrm{se}}} = \frac{2j}{D\,(c - c_{\mathrm{se}})/L_{\mathrm{s}}} = \frac{140}{17} \approx 8.2, \tag{39}$$

where $c_{\mathrm{se}}$ is the concentration at the spacer-electrode interface at $y = \pm L_{\mathrm{s}}/2$. For plug flow $\mathrm{Sh}_{\mathrm{s}} = 12$ [39]. Note that in the definition of the Sherwood number, Eq. (39), the flux towards both both sides is included. Combining Eqs. (37) and (39)

$$UL_{\mathrm{s}}\frac{dc}{dx} = -2j = -D\mathrm{Sh}_{\mathrm{s}}\frac{c - c_{\mathrm{se}}}{L_{\mathrm{s}}}. \tag{40}$$

### 4.2. Concentration profile

Satisfying Eq. (31) ensures that the macropore concentration will initially vanish. The adsorption will then take place in a relatively localized part of the porous electrode where there is still some capacity for adsorption $\bar{w}_{\mathrm{m}} < \bar{w}_{\max}$ and there is some salt in the macropores. This leads to the salt shocks discussed in the introduction. Diffusion of salt from the channel will give rise to a linearly decreasing concentration profile up the shock location $y = L_{\mathrm{s}}/2 + \zeta L_{\mathrm{e}}$ as displayed in Fig. 6. This

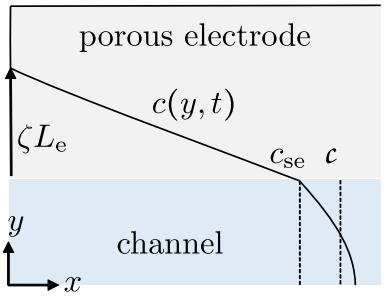


**Fig. 6.** The idealized concentration profile used in the analytical model. Inside the porous electrode the concentration decreases linearly up to a depth $\zeta L_e$ as described by Eq. (41). In the channel, the fully developed concentration profile will be approximately parabolic.

idealized concentration profile is parametrized by[13]

$$c(y,t) \approx \begin{cases} c_{se} + \frac{5}{4}(c - c_{se})\left(1 - \left(\frac{y}{L_s/2}\right)^2\right) & |y| < L_s/2 \\ c_{se}\left(1 - \frac{|y| - L_s/2}{\zeta L_e}\right) & L_s/2 \le |y| < L_s/2 + \zeta L_e \\ 0 & |y| \ge L_s/2 + \zeta L_e. \end{cases} \tag{41}$$

The assumption of a parabolic profile in the channel is of no consequence and will only be used for visualization purposes.

### 4.3. Electrode

Inside the electrode at $y = L_s/2$, Eq. (41) gives $\frac{\partial c}{\partial y} = -\frac{c_{se}}{\zeta L_e}$ so that the salt flux inside the porous electrode $j = -D_e\frac{\partial c}{\partial y}$ reads

$$j = D_e\frac{c_{se}}{\zeta L_e}. \tag{42}$$

Before the adsorption front, at locations closer to the spacer, we assume the micropore ion density is at its maximum $w_{max}$ while beyond the front it is at its initial value $w_0$. Therefore, with $w \equiv w_{max} - w_0$ constant, conservation of salt allows us to write[14]

$$j = 2wp_m L_e\frac{\partial\zeta}{\partial t}. \tag{43}$$

Combining Eqs. (42) and (40) gives

$$j = D_e \mathrm{Sh}\frac{c}{L_e}, \tag{44}$$

where

$$\mathrm{Sh}^{-1} = \widetilde{\mathrm{Sh}}^{-1} + \zeta \tag{45}$$

with Sh the overall Sherwood number and

$$\widetilde{\mathrm{Sh}} \equiv \frac{\mathrm{Sh}_s D L_e}{2L_s D_e}, \tag{46}$$

the spacer Sherwood number based on the electrode properties. The 2 appears here because the channel Sherwood number of Eq. (39) was based on flux towards two sides. When $\tilde{\mathrm{Sh}} \ll 1/\zeta$ the mass transfer resistance of the electrode can be neglected. When $\tilde{\mathrm{Sh}} \gg 1/\zeta$ the mass transfer resistance in the spacer can be neglected. Eq. (44) describes the flux of concentration from $c$ in the channel to 0 at the desalting front. The overall dimensionless mass transport resistance $\mathrm{Sh}^{-1}$ is formed by the sum of a mass transfer resistance $\tilde{\mathrm{Sh}}^{-1}$ in the channel and $\zeta$ in the electrode. The latter increases as time-evolves and the desalting front moves deeper into the electrode but is limited to a maximum of unity. With the numbers in Table 1 and $\mathrm{Sh} = 140/17$ from Eq. (39) we have $\tilde{\mathrm{Sh}} \approx 7$. Therefore, initially the main mass transport limitation may be in the channel, but as $\zeta$ increases towards 1, the main mass transport limitation will be in the electrode in this case. We can derive from Eqs. (42), (44) and (45) that

$$c_{se} = \frac{c}{1 + \frac{1}{\zeta\tilde{\mathrm{Sh}}}}. \tag{47}$$

Initially, when $\zeta = 0$ this gives $c_{se} \approx 0$. In the limit $\zeta\tilde{\mathrm{Sh}} \gg 1$ of negligible channel mass transfer limitations we have $c_{se} = c$.

### 4.4. Ohmic drop

In the negative electrode primarily cations are transported while $j_- \approx 0$ so we have a Boltzmann distribution $\Delta\bar{\phi} = \Delta\ln(c)$. Inserting the idealized profile of Eq. (41) gives for the potential drop over the electrode up to $y$ a value $\Delta\bar{\phi} = \ln\frac{c(y)}{c_{se}}$. Close to the spacer this can be linearized to give $\Delta\bar{\phi} \approx \frac{|y| - L_s/2}{\zeta L_e}$. Extrapolating this approximation to the desalting front at $|y| = L_s/2 + \zeta L_e$ we obtain $\Delta\bar{\phi} \approx 1$ as a rough approximation for the total ionic ohmic drop over the electrode.[15] For the potential drop over the spacer we will use Ohm's law to give $\Delta\phi \approx \frac{jFL_s}{\langle\kappa\rangle}$ where $\langle\kappa\rangle \approx \frac{2F^2D}{RT}c$ similar to Eq. (15). Referring to Fig. 2, the ohmic drop $\Delta\phi_\Omega$ consists of a drop over the electrode as well as half the channel, so that

$$\Delta\phi_\Omega \approx \frac{RT}{F} + \frac{jFL_s/2}{\langle\kappa\rangle} = \frac{RT}{F}\left(1 + \frac{jL_s}{4Dc}\right). \tag{48}$$

With Eqs. (44) and (46) this gives

$$\Delta\bar{\phi}_\Omega \sim 1 + \frac{\mathrm{Sh}}{2}\frac{D_e L_s}{D L_e} = 1 + \frac{\mathrm{Sh}_s/4}{1 + \tilde{\mathrm{Sh}}\zeta}. \tag{49}$$

Using the values in Table 1 and $\mathrm{Sh}_s \approx 8$ for Poiseuille flow, this gives $\Delta\bar{\phi}_\Omega \sim 1 + \frac{2}{1+7\zeta}$. For $\zeta \ge 1/7$ the spacer ohmic drop contribution to $\Delta\bar{\phi}_\Omega$, the second term in Eq. (49), will be smaller than that of the electrode, the first term.

Note that with the assumption of zero macropore concentration beyond the shock, we consider mass-transfer limited operation at the limiting current density. In this case the flux cannot be increased by increasing the cell potential, because the macropore salt concentration vanishes at the location of the adsorption front and the rate of diffusion becomes limiting. Our Eq. (42) for the flux does not include the cell potential, in contrast with for example Eq. (9) of Ref. [47], Eq. (17) of Ref. [49], or Eq. (4) of Ref. [67]. There will be a potential drop over the spacer, but this solely cannot be used to determine the flux under the present mass-transport limiting conditions. Our model thus equally describes both approximately constant current as well as approximately constant voltage operation. Note that this does not mean that the cell

[13] The prefactor 5/4 comes from Eq. (38) using $u(y) = \frac{3U}{2}\left(1 - \left(\frac{y}{L_s/2}\right)^2\right)$. Approximating the concentration profile with a parabolic profile it can be derived that the average concentration is given by $\frac{5}{6}c + \frac{1}{6}c_{se}$. We content ourselves with using the cup-mixing average $c$ instead.

[14] Eq. (7) in dimensional form, $p_M\frac{\partial c}{\partial t} = p_M D_e\nabla^2 c - p_m\frac{\partial w_m}{\partial t}$, upon integrating over the electrode thickness from $y = L_s/2$ to $y = L_s/2 + L_e$ gives $p_M V\frac{d\langle c\rangle}{dt} = jA/2 - p_m V\frac{d\langle w_m\rangle}{dt}$. Here brackets denote $y$-averages and we used the divergence theorem to give $p_M\int D_e\nabla^2 c dV = p_M\int D_e\nabla c\cdot d\mathbf{A} = jA/2$ for the influx of salt into the electrode. With $w$ constant we can write $\frac{d\langle w_m\rangle}{dt} = w\frac{d\zeta}{dt}$ and with $\bar{w}_m \gg 1$ we can neglect the left-hand side and obtain Eq. (43).

[15] As the concentration tends to zero near the desalting zone the potential drop diverges. However, the assumption of a Boltzmann distribution also breaks down here and an accurate evaluation of the ohmic drop requires a more careful consideration.

voltage has no influence in our model. Through Eq. (33) it influences $w$, which impacts the time dynamics through Eq. (43). A higher cell voltage means a higher $w$ so that $\zeta$ increases slower and the flux can be kept higher for longer.

### 4.5. Initial condition

Fig. 4(a) and (c) shows that within one diffusional time $\bar{t}\lesssim 1$ all of the salt in the macropores has entered the micropores. This salt is adsorbed almost all near the entrance where the largest potential difference arises for adsorption. Since this occurs over the short diffusional time-scale not included in our model, we will model this as an initial condition for $\zeta$.

The number of moles of ions of either charge in the macropores $2p_{\mathrm{M}}Vc_0$ divided by the micropore volume $p_{\mathrm{m}}V$ gives a micropore ion concentration $2w_{\mathrm{m},0} = 2c_0p_{\mathrm{M}}/p_{\mathrm{m}}$. Of the total available adsorption capacity $w$ a fraction

$$\zeta_0 = \frac{w_{\mathrm{m},0}}{w} = \frac{p_{\mathrm{M}}/p_{\mathrm{m}}}{\bar{w}}, \tag{50}$$

is immediately taken up by salt adsorbed from the macropores. Using the numbers from Table 1 we obtained $\bar{w} = 13$ for $\bar{V} = 40$ just below Eq. (33) giving $\zeta_0 \approx 0.1$. So, in this case of the maximum $\bar{w}_{\max} = 18$ about $\bar{w}_0 = 4.5$ is removed due to non-electrostatic adsorption, leaving $\bar{w} = 13$. After a time $t > t_{RC}$ the co-ions are all expelled and traded for counter-ions. After a time $t > t_D$ the salt in the macropores has entered the micropores as well, subtracting another $\bar{w}_{\mathrm{m},0} \approx 1.35$ on average, but primarily near the front of the electrodes.

### 4.6. Dimensionless equations

The resulting analytical model consists of Eqs. (40), (44) and (43), or

$$j = -\frac{UL_{\mathrm{s}}}{2}\frac{dc}{dx} = \frac{D_{\mathrm{e}}c/L_{\mathrm{e}}}{\tilde{\mathrm{Sh}}^{-1} + \zeta} = 2wp_{\mathrm{m}}L_{\mathrm{e}}\frac{\partial\zeta}{\partial t}, \tag{51}$$

where $w$ is given by Eq. (33). These equations can be written as

$$\frac{\partial\bar{c}}{\partial\tilde{x}} = -\frac{\bar{c}}{1+\tilde{\zeta}}, \tag{52}$$

$$\frac{\partial\tilde{\zeta}}{\partial\tilde{t}} = \frac{\bar{c}}{1+\tilde{\zeta}}. \tag{53}$$

in terms of the dimensionless flux or current density

$$\bar{j} \equiv \frac{jL_{\mathrm{e}}}{D_{\mathrm{e}}\tilde{\mathrm{Sh}}c_0} = \frac{\bar{c}}{1+\tilde{\zeta}}. \tag{54}$$

here $\tilde{\zeta} = \tilde{\mathrm{Sh}}\zeta$, $\tilde{x} = \frac{\tilde{\mathrm{Sh}}_{\mathrm{s}}}{\mathrm{Gz}}\bar{x}$, and $\tilde{t} = \frac{\tilde{\mathrm{Sh}}^2}{2wp_{\mathrm{m}}}\bar{t}$, where $\bar{x} = \frac{x}{L}$ and $\bar{t} = \frac{D_{\mathrm{e}}}{L_{\mathrm{e}}^2}t$, or

$$\widetilde{\zeta} = \frac{\mathrm{Sh}_{\mathrm{s}}DL_{\mathrm{e}}}{2L_{\mathrm{s}}D_{\mathrm{e}}}\zeta, \tag{55}$$

$$\widetilde{x} = \frac{D\mathrm{Sh}_{\mathrm{s}}}{UL_{\mathrm{s}}^2}x, \tag{56}$$

$$\widetilde{t} = \frac{c_0}{8wp_{\mathrm{m}}D_{\mathrm{e}}}\left(\frac{\mathrm{Sh}_{\mathrm{s}}D}{L_{\mathrm{s}}}\right)^2 t. \tag{57}$$

In writing Eqs. (56) and (57) we considered $\bar{w}$ to be a constant. In general we may use $\tilde{x} = \int\frac{\tilde{\mathrm{Sh}}_{\mathrm{s}}}{\mathrm{Gz}}d\bar{x}$ and $\tilde{t} = \int\frac{\tilde{\mathrm{Sh}}^2}{2p_{\mathrm{m}}w}d\bar{t}$.[16] Note from Eq. (45) that $\tilde{\zeta} = \zeta/\tilde{\mathrm{Sh}}^{-1}$ is the ratio of the electrode and channel mass transfer resistances. For small values $\tilde{\zeta}\ll 1$ the mass transfer resistance lies in the channel, while for $\tilde{\zeta}\gg 1$ the electrode becomes the limiting factor.

The first order system of Eqs. (52) and (53) will be accompanied by

$$\bar{c}(\tilde{x}=0) = 1, \tag{58}$$

$$\tilde{\zeta}(\tilde{t}=0) = \tilde{\zeta}_0, \tag{59}$$

as boundary and initial conditions, respectively. From Eq. (50):

$$\tilde{\zeta}_0 = \widetilde{\mathrm{Sh}}\frac{p_{\mathrm{M}}/p_{\mathrm{m}}}{\bar{w}}. \tag{60}$$

For the numbers in Table 1 we find $\zeta_0 \approx 0.1$. Therefore, the initial macro-pore concentration, which during the *RC*-time enters the micropores near the spacer, will result in charging about 10 % of the electrode initially. However, since $\tilde{\mathrm{Sh}} \approx 7$ this gives $\tilde{\zeta}_0 \approx 0.7$. In this case, even 10 % charging gives a significant mass transfer resistance in the electrodes. Through the numerator of Eqs. (52) and (53) this $\tilde{\zeta}_0 \approx 0.7$ will have a non-negligible impact on the time-evolution. For substantially lower salt concentrations,[17] typically $\tilde{\zeta}_0 \ll 1$ so $\tilde{\zeta}_0 = 0$ may be used as an approximate initial condition.

## 5. Analytical solutions

### 5.1. Exact solution

Under the assumptions outlined in Section 3 we managed to reduce the computational model of Section 2 to two coupled partial differential Eqs. (52) and (53) for the dimensionless cup-mixing average channel concentration $\bar{c}$ and electrode to channel mass-transfer resistance ratio $\tilde{\zeta} = \tilde{\mathrm{Sh}}\zeta$, with boundary condition (Eq. (58)) and initial condition (Eq. (59)). Although rarely the case for coupled partial differential equations, this problem admits an exact analytical solution, derived in Appendix B:

$$\frac{\tilde{\zeta} - \tilde{\zeta}_0}{1+\tilde{\zeta}_0} = \hat{t}\bar{c} = \mathrm{W}\left(\hat{t}\mathrm{e}^{\hat{t}-\frac{\tilde{x}}{1+\tilde{\zeta}_0}}\right), \tag{61}$$

where we introduced a new dimensionless time

$$\hat{t} \equiv \sqrt{1 + \frac{2\tilde{t}}{(1+\tilde{\zeta}_0)^2}} - 1, \tag{62}$$

that reduces to $\tilde{t}$ when $\tilde{t}\ll 1$. Note that the effect of $\tilde{\zeta}_0$ on $\bar{c}$ is to replace $\tilde{x}\to\frac{\tilde{x}}{1+\tilde{\zeta}_0}$ and $\tilde{t}\to\frac{\tilde{t}}{(1+\tilde{\zeta}_0)^2}$. The effect on $\tilde{\zeta}$ is that $\tilde{\zeta}\to\frac{\tilde{\zeta}-\tilde{\zeta}_0}{1+\tilde{\zeta}_0}$. Therefore, from now on we will simplify Eq. (61) using $\tilde{\zeta}_0 = 0$ knowing that we can always recover from the below equations and approximations the more general result by making these substitutions. For $\tilde{\zeta}_0 = 0$, Eq. (61) becomes

$$\tilde{\zeta} = \hat{t}\bar{c} = \mathrm{W}\left(\hat{t}\mathrm{e}^{\hat{t}-\tilde{x}}\right), \tag{63}$$

where

$$\hat{t} \equiv \sqrt{1+2\tilde{t}} - 1, \tag{64}$$

tends to $\hat{t}\approx\tilde{t}\ll 1$ for small times and $\hat{t}\approx\sqrt{2\tilde{t}}\gg 1$ for large times. Note from Eq. (63) that $\tilde{\zeta}$ and $\bar{c}$ will have the same shape, and only a magnitude difference depending on time. This is illustrated in Fig. 7, which graphically shows the analytical solution of Eq. (63). That $\bar{c}/\tilde{\zeta}$ depends only on time implies, by Eqs. (52) and (54), that the

[16] The decrease in channel concentration in the streamwise direction cam have an impact on the ohmic drop and therefore $\bar{w}$. The salt concentration can influence the capacitance, which increases with increasing micropore charge density [48]. The parameter $w$ only enters $\tilde{t}$ and, therefore such spatial effects can only be included in our model very crudely by making $w$ depend on time.

[17] Or higher capacitance electrodes, which will equally increase $\bar{w}$ and decrease $\tilde{\zeta}_0$. Also a larger spacer to electrode thickness ratio $L_{\mathrm{s}}/L_{\mathrm{e}}$, through a decrease in $\tilde{\mathrm{Sh}}$, can make $\tilde{\zeta}_0\ll 1$.

dimensionless current density $\bar{j} = -\partial\bar{c}/\partial\tilde{x}$ is spatially constant when $\tilde{\zeta}\gg 1$.

With $\frac{dW(x)}{dx} = \frac{1}{x}\frac{W(x)}{1+W(x)}$ it can be verified by insertion that Eq. (61) satisfies Eqs. (52), (53), (58) and (59). In Appendix C a numerical verification is provided. The used Matlab code is provided for general as a supporting file. It may be extended to incorporate for example variable properties or different boundary conditions.

### 5.2. Approximations to the exact solution

The exact solution of Eq. (63) will require evaluation of the Lambert W function. In case the desired software or coding environments does not have the Lambert W function available it can be easily programmed through a root-solver using its definition, Eq. (27), or approximated by Eq. (A.1). To gain more insight into the analytical solution, here we consider further simplifications that are possible for small and large $\tilde{t}$. Using the approximation $W(x) \approx x \ll 1$ of Appendix A, for small times $\hat{t} \approx \tilde{t} \ll 1$ so that the mass-transfer resistance of the electrode can be neglected, we obtain

$$\bar{c} \approx \frac{\tilde{\zeta}}{\tilde{t}} = e^{-\tilde{x}}. \tag{65}$$

A more accurate approximation is obtained by integrating Eq. (53) assuming $\bar{c} = 1$ to give $\tilde{\zeta} = \tilde{t}$. Integrating Eq. (52), assuming $\tilde{\zeta}$ is independent of time, gives $\bar{c} = e^{-\frac{\tilde{x}}{1+\tilde{\zeta}}}$ so that

$$\bar{c} \approx \frac{\tilde{\zeta}}{\tilde{\delta}-1} = e^{-\frac{\tilde{x}}{\tilde{\delta}}}, \tag{66}$$

where the e-folding length-scale $\tilde{\delta} = 1 + \tilde{t}$, or

$$\tilde{\delta} = \sqrt{1+2\tilde{t}}. \tag{67}$$

For $\hat{t} \ll 1$ the concentration profile will be independent of time. We note that an inlet velocity that decreases in time according to $U = U_0/\sqrt{1+2\tilde{t}}$ cancels the time dependence in $\hat{x}/\hat{\delta}$ so that the concentration profile remains steady. This may be an advantageous operating regime, for example when there are limitations on the possible channel length. Since we derived our model with a constant velocity in mind, this operating strategy remains to be verified.

In general, for large times $\hat{t} \gg 1$ we can use the approximation $W(x) \approx \ln x \gg 1$ of Appendix A so that, neglecting $\ln\hat{t}$ relative to $\hat{t}$, Eq. (63) gives $\tilde{\zeta} \approx \hat{t} - \tilde{x}$. To retain approximate validity also for $\hat{t} = 0$ we slightly modify this to $\tilde{\zeta} \approx \hat{t}(1 - \tilde{x}/\tilde{\delta})$, using that for large values of $1 \ll \hat{t} = \tilde{\delta} - 1 \approx \tilde{\delta}$. Therefore, $\tilde{\zeta} = \hat{t}\,\bar{c}$ gives

$$\bar{c} \approx \frac{\tilde{\zeta}}{\tilde{\delta}-1} \approx \begin{cases} 1 - \tilde{x}/\tilde{\delta} & \tilde{x} < \tilde{\delta}, \\ 0 & \tilde{x} \geq \tilde{\delta}. \end{cases} \tag{68}$$

This is a linear profile decreasing over a length-scale $\tilde{\delta}$. Note that for $\tilde{x} \ll \tilde{\delta}$ and $\tilde{x} \gg \tilde{\delta}$ Eq. (68), valid for $\tilde{t} \gg 1$, agrees with Eq. (66), valid for $\tilde{t} \ll 1$. The approximations obtained in this section confirm the observation from Fig. 6 that the profile evolves from an approximately exponential profile for small times to a more or less linear profile for large times. They compare well with the exact solution, as shown in Figs. 7 and 8. We do note that the linear profile approximation of Eq. (68) for $\tilde{t}$ becomes inaccurate for low concentrations $\bar{c} \lesssim 0.2$. Therefore it can only be used with good accuracy when

$$\tilde{x} \lesssim 0.8\tilde{\delta} \text{ or } \tilde{x} \gg \tilde{\delta}. \tag{69}$$

For intermediate values up to $\tilde{t}$ of the order $10^2$, Eqs. (66) and (D.4) give better agreement near $\tilde{x} \approx \tilde{\delta}$ as shown in Fig. D.14.

#### 5.2.1. Charged approximation

No more salt can be adsorbed and the electrode is locally 'fully charged' when $\zeta = \tilde{\zeta}/\tilde{Sh} = 1$. Eq. (63) for $\tilde{\zeta} = \tilde{Sh}$ and $\tilde{x} = 0$ reads $\tilde{Sh} = W(\hat{t}e^{\hat{t}})$. From the defining relation of the Lambert W function, Eq. (27), this is automatically solved by $\hat{t} = \tilde{Sh}$. Therefore, after a charging time

$$\tilde{t}_c \equiv \widetilde{Sh}(1 + \widetilde{Sh}/2), \tag{70}$$

the electrode will be fully-charged near the inlet. Solving Eq. (63) for $\tilde{\zeta} = \tilde{Sh}$ gives for $\tilde{x} = \tilde{x}_c$

$$\tilde{x}_c = \hat{t} - \widetilde{Sh} + \ln\frac{\hat{t}}{\widetilde{Sh}}. \tag{71}$$

This will give an indication of up to where the electrode is fully charged. The electrode upstream of this point will be already fully charged but the effect of this is not included in the analytical solution. Therefore, this is will be an under-prediction and can only be used as a rough approximation. The electrode will be fully charged when $\tilde{x}_c \approx \tilde{L}$. Eq. (71) can be solved for the time $\hat{t} = \hat{t}_{c,L}$ that this happens, to give

$$\hat{t}_{c,L} = W\left(\hat{L}e^{\tilde{L}+\tilde{Sh}}\right). \tag{72}$$

Within the rough present 'charged-approximation' this time $\hat{t}_{c,L}$ will give an indication of when the whole electrode will be fully charged.[18]

After a time $\tilde{t}_c$, given by Eq. (70), a growing region near the inlet will be fully charged and effectively useless for desalination.[19] Therefore, *we can at this time effectively move the inlet towards the position* $\tilde{x} = \tilde{x}_c$ since between $\tilde{x} = 0$ and $\tilde{x}_c$ the channel concentration will remain approximately equal to the inlet concentration. We expect that Eq. (63), upon replacing $\tilde{x}$ with $\tilde{x} - \tilde{x}_c$, will approximately remain to hold for $\tilde{x} > \tilde{x}_c$ and $\tilde{t} > \tilde{t}_c$.[20] For large $\hat{t} \gg 1$ we can use Eq. (68) to give $\bar{c} \approx 1 - \frac{\tilde{x}-\tilde{x}_c}{\tilde{\delta}}$. To summarize, we have

$$\frac{\tilde{\zeta}-\tilde{\zeta}_0}{1+\tilde{\zeta}_0} \approx \begin{cases} W\left(\hat{t}e^{\hat{t}-\frac{\tilde{x}}{1+\tilde{\zeta}_0}}\right) & \tilde{x}_c < 0 \\ \dfrac{\widetilde{Sh}-\tilde{\zeta}_0}{1+\tilde{\zeta}_0} & \tilde{x} < \tilde{x}_c \\ W\left(\hat{t}e^{\hat{t}-\frac{\tilde{x}-\tilde{x}_c}{1+\tilde{\zeta}_0}}\right) & \tilde{x} > \tilde{x}_c > 0 \end{cases} \tag{74}$$

and

$$\bar{c} \approx \begin{cases} W\left(\hat{t}e^{\hat{t}-\frac{\tilde{x}}{1+\tilde{\zeta}_0}}\right)/\hat{t} & \tilde{x}_C < 0 \\ 1 & \tilde{x} < \tilde{x}_C \\ W\left(\hat{t}e^{\hat{t}-\frac{\tilde{x}-\tilde{x}_C}{1+\tilde{\zeta}_0}}\right)/\hat{t} & \tilde{x} > \tilde{x}_C > 0 \end{cases} \tag{75}$$

where $\tilde{t}$ in general is given by the definition in Eq. (62), $\tilde{x}_c$ by Eq. (71). In Eq. (75) we leave the option open to use a different $\tilde{x}_C \equiv \tilde{x}_c(t - t_{lag}) < \tilde{x}_c$

[18] Note that for $\hat{L} \gg \tilde{Sh}$, Eq. (27) gives $\hat{t}_{c,L} = \tilde{L} + \tilde{Sh}$, in agreement with neglecting the logarithm in Eq. (71). For $\hat{L} \ll 1$ Eq. (72) can be approximated by $\hat{t}_{c,L} = \hat{L}e^{\tilde{Sh}}$.

[19] This process can be relatively easily modelled numerically by checking for what $x$ it holds that $\zeta(x, t - t_D) \geq 1$ and setting $\bar{c} = 1$, moving the inlet condition to a new position where $\zeta(x, t - t_D) = 1$. Note that the introduction of the criterion $\zeta = \tilde{\zeta}/\tilde{Sh} = 1$ introduces an additional variable $\tilde{Sh}$ into the model. A time-lag $t = t_D$ equates to a dimensionless time $\bar{t} = 1$ or $\tilde{t} = \tilde{Sh}^2/p_m\bar{w}$, introducing again an additional variable $p_m\bar{w}$ to the model.

[20] Replacing $\tilde{x}$ with $\tilde{x} - \tilde{x}_c$ in Eq. (63) gives $\bar{c} = \tilde{\zeta}/\hat{t}$ where

$$\tilde{\zeta} \approx W\left(\hat{t}^2 e^{2\hat{t}-\tilde{x}-\tilde{Sh}}/\widetilde{Sh}\right). \tag{73}$$

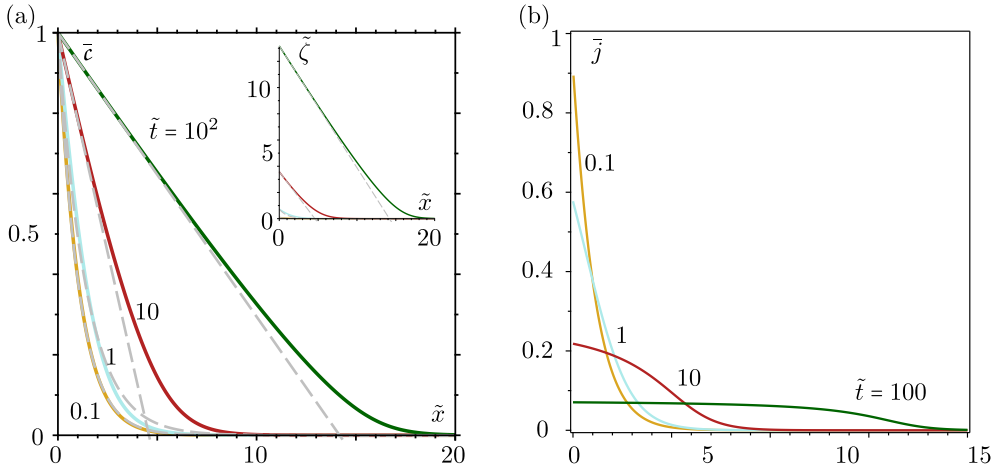


**Fig. 7.** (a) The exact analytical solution (solid curves) for the dimensionless concentration $c$ and mass-transfer ratio $\tilde{\zeta} = \widehat{t}\overline{c}$ (inset) of Eq. (63) is compared with the approximations (grey dashed lines) of Eq. (66) for $\tilde{t} = 0.1$ and 1 and with the approximations of Eq. (68) for $\tilde{t} = 10$ and 100. (b) The dimensionless current density $\bar{j} = \frac{jL_e}{D_e \tilde{\mathrm{Sh}} c_0} = \frac{\bar{c}}{1+\zeta}$ of Eq. (54) becomes spatially constant and equal to $\bar{c}/\tilde{\zeta} \approx 1/\widehat{t}$ for $\tilde{\zeta} \gg 1$ according to Eqs. (63) and (64), when the mass transfer resistance in the channel dominates over that in the channel.

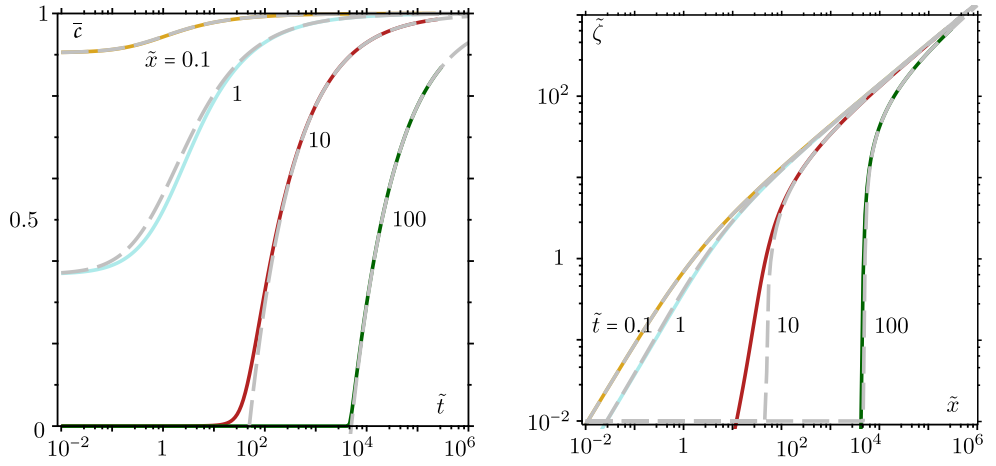


**Fig. 8.** The exact analytical solution (solid curves) for the dimensionless concentration $\bar{c}$ (left) and mass-transfer ratio $\tilde{\zeta} = \widehat{t}\overline{c}$ (right) of Eq. (63) is compared with the approximations (grey dashed lines) of Eq. (66) for $\tilde{x} = 0.1$ and 1 (left) and $\tilde{t} = 0.1$ and 1 (right) and with the approximations of Eq. (68) for $\tilde{x} = 10$ and 100 (left)and $\tilde{t} = 10$ and 100 (right).

to account for a time-lag $t_{\mathrm{lag}}$ between the electrode being fully charged and the concentration in the channel being affected. This time-lag is primarily due to the time it takes for the macropore concentration to equilibrate by diffusion. Therefore, we may take $t_{\mathrm{lag}} \sim t_D$, as we will do in the next section. See however Appendix E for more detailed considerations. In the next section, we will compare the analytical solutions discussed in this section with those of the full model discussed in Section 2.

## 6. Model verification

Here we will compare the exact solution of Eqs. (74) and (75) with a comprehensive 2D transient COMSOL model based on the general equations outlined in Section 2.2, see also Appendix I. Unless stated otherwise, the parameters in Table 1 are used, which are equal to those in Ref. [27]. Eqs. (33) and (49) then give the values for $\bar{w}$ reported in Table 2. The dimensionless times $\bar{t}_{RC} = \frac{p_{\mathrm{m}}}{p_{\mathrm{M}}}\bar{C}_{\mathrm{m}} = 0.75$ and $\bar{t}_U = \frac{\bar{L}_s^2}{\mathrm{Gz}\bar{D}} = 0.47$. The simulation results for times $\bar{t} \lesssim 1$ have been discussed in Fig. 4. Here we focus on times $\bar{t} \gtrsim 1$ so the criteria of Eq. (19), $\bar{t} \gtrsim 1, \bar{t}_{RC}, \bar{t}_U$ are satisfied.

### 6.1. Spatial profiles

In Fig. 9 we compare the halfway-the-channel concentration profiles

**Table 2**
Dimensionless parameters used in comparing the COMSOL simulations with the analytical solutions. The approximate dimensionless voltages correspond to $V_{\mathrm{ext}} \approx 0.8$, 1, and 1.2 V at $T = 293.15$ K. Here $\bar{w}$ is obtained from Eq. (33) using the parameters in Table 1 and neglecting the ohmic drop, taking $\Delta\phi_\Omega = 0$. Eq. (70) gives $\tilde{t}_{\mathrm{c}} = 31.5$ so that $\bar{t}_{\mathrm{c}} = \frac{2\bar{w}p_{\mathrm{m}}}{\tilde{\mathrm{Sh}}^2}\widehat{t}_{\mathrm{c}} \approx 0.4\bar{w}$. Eq. (50) gives $\zeta_0 = \frac{4}{3\bar{w}}$ so $\tilde{\zeta}_0 = \tilde{\mathrm{Sh}}\zeta_0 \approx 7\zeta_0$.

| $\bar{V}_{\mathrm{ext}}$: | 32 | 40 | 48 |
|---|---|---|---|
| $\bar{w}$ | 9.3 | 13 | 17 |
| $\bar{t}_{\mathrm{c}}$ | 3.9 | 5.2 | 6.5 |
| $\zeta_0$ | 0.14 | 0.1 | 0.08 |

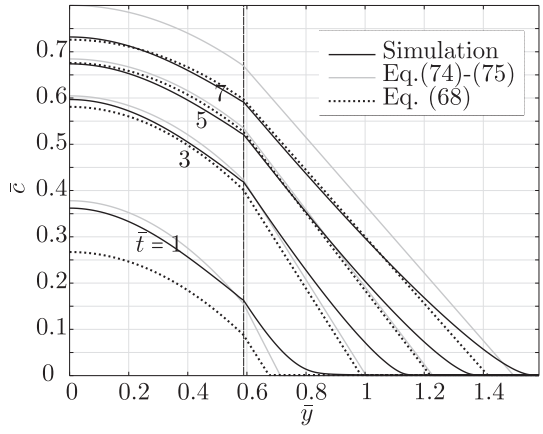


**Fig. 9.** Comparison of the dimensionless concentration $\bar{c}$ between simulation and the analytical solution of Eq. (41), including the charging approximation (Eqs. (74)–(75)), and the approximate solution (Eq. (68)) halfway the channel at $x = L/2$ and $\bar{V}_{\text{ext}} = 40$, using the parameters in Tables 1 and 2. The respective profiles in the spacer and electrode are determined through Eq. (41).

from COMSOL simulations with the analytical profile of Eq. (41) using $\tilde{\zeta}$ and $\bar{c}$ from Eqs. (74) and (75), respectively. In Fig. 10 we provide the same results as 2D colour plots for the whole channel. Very good agreement can be seen for $\bar{t} = 1, 3$ and 5. The analytical model assumes an infinitely thin salt adsorption zone, or desalination shock, resulting in linear concentration profiles inside the electrodes. The COMSOL models show a more extended adsorption zone, resulting in small deviations from the linear concentration profile. For $\bar{t} = 7$, the electrode can be seen to be fully charged near the inlet, which increase the channel concentration. The 'charged approximation' of Section 5.2.1 clearly is less accurate in this phase, and the errors increase. In Fig. 9 we also included the linear approximation of Eq. (68) without the charged approximation. Since strictly only valid for $\tilde{t} \gg 1$ it does less well than the exact solution for $\bar{t} = 1$. Fortuitously, for the $\bar{t} = 7$ curve, not including the charged approximation improves the agreement for this particular case.

### 6.2. Outlet concentration

Fig. 11(a) shows the outlet concentration as a function of time for various applied potentials $\bar{V}_{\text{ext}}$ and Fig. 11(b) for various channel lengths compared to $L$ used in the other simulations. We see that around $\bar{t} \sim \bar{t}_U = 0.47$ the outlet concentration starts to increase in time, and the agreement with the analytical result of Eq. (75) becomes very good. After this transit time sometimes a "plateau region" can be seen [27]. Most of our simulations, except for the $4L$ case in Fig. 11(b), do not show such a constant low outlet concentration regime because the channel length was chosen relatively small.

Eq. (70) predicts that around $\tilde{t}_c \approx \tilde{\text{Sh}}(1 + \tilde{\text{Sh}}/2) = 31.5$ the electrode near the inlet becomes fully saturated and reaches $\zeta = 1$. Adding the diffusion time lag $t_{\text{lag}} \sim t_D$, Table 2 shows that the channel concentration is impacted between $5 \lesssim \bar{t}_c + 1 \lesssim 7.5$ in the voltage range $32 \leq \bar{V} \leq 48$. From this time onwards, in the analytical solution the inlet is effectively placed at the location up to where the electrode is fully saturated, as discussed in Section 5.2.1. This results in the trend change visible between $\bar{t} = 5$ and 7.5 in Fig. 11(a). Note that for the longest channel, when the outlet concentration can be seen to increase, the electrode near the inlet is already fully charged.[21] Therefore, only the analytical charged approximation is visible in this case.

Fig. 12 shows how the analytical model also predicts quite well the location of the adsorption shock front where the macropore concentration approximately vanishes.

With the analytical solution Eq. (61) of our simplified model Eqs. (52) and (53) sufficiently verified, in the next section we will use these relations to optimize various geometrical and operational parameters.

## 7. Optimization

Many metrics exists in the literature that can be used to compare the performance of different CDI experiments [25]. The analytical solution of the previous section, Eq. (61) and its approximations of Eqs. (66) and (68), will allow us to evaluate these metrics analytically. In this way the relation between geometrical and operational parameters and performance can be studied.

Both the approximation of Eq. (66) for small $\tilde{t}$ and the concentration profile of Eq. (68) for large dimensionless times depend only on the variable $\tilde{x}/\tilde{\delta}$. For convenience we here summarize these main results

$$\bar{c} \approx \begin{cases} e^{-\tilde{x}/\tilde{\delta}} & \tilde{t} \ll 1 \\ 1 - \tilde{x}/\tilde{\delta} & \tilde{t} \gg 1, \tilde{x} \leq \tilde{\delta} \end{cases} \tag{76}$$

where we note that for rough engineering calculations both equations may suffice for any time.

We have thus managed to find an approximate solution that depends only on[22]:

$$\frac{\tilde{x}}{\tilde{\delta}} = \frac{\tilde{x}}{\sqrt{1+2\tilde{t}}} = \frac{\bar{x}t_U/t_s}{\sqrt{1+\frac{\tilde{\text{Sh}}^2}{\bar{w}p_m}\bar{t}}} = \frac{x/U}{\sqrt{\left(\frac{L_s^2}{\text{Sh}_s D}\right)^2 + \frac{L_s^2}{4D_e}\frac{t}{p_m \bar{w}}}}, \tag{77}$$

where we introduced the characteristic diffusion time-scale for the spacer $t_s \equiv L_s^2/\text{Sh}_s D$ in terms of which[23] $\tilde{x} = \frac{t_U}{t_s}\bar{x}$. For $\tilde{t} \ll 1$, the spatial variation depends only on $\tilde{x} = \bar{x}t_U/t_s$, proportional to the number of transit-times that fit into one spacer diffusion time. When $\tilde{t}$ is no longer small, the mass transfer resistance in the electrodes starts to play a role and will modify this spatial variation.

As further discussed in Appendix F, there are many metrics that can be optimized. Here, we give priority to maintaining a low salt outlet concentration throughout the charging cycle, maximal productivity or flow rate per unit area, and minimal specific energy dissipation.

[21] Note that in Fig. 11(b) the value for $\bar{w}$, and therefore the time at which the electrode is charged near the inlet, is the same for all curves. However, the COMSOL results show a visible trend change later for longer channels. This can be only in small part attributed to the time-lag $t_U = L/U$ for the impacted flow near the inlet to reach the outlet, since for $L = 4$ the transit time halfway the channel $\bar{t}_U/2 \approx 1$. To a larger degree it seems that the transition to the charged approximation becomes more smeared out for larger $L$.

[22] There are a few things to note that make things slightly more complicated: 1) unless it is small compared to 1 the value of $\tilde{\zeta}_0$ will also play some role 2) For small to moderate $t/t_U$, the time-scale $t_U$ will also play a role, as discussed in H. 3) When the desalting front reaches the end of the electrode the additional time-scale $\tilde{t}_c = \tilde{\text{Sh}}(1 + \tilde{\text{Sh}}/2)$ of Eq. (70) enters the solution, approximately in the form of Eqs. (74)–(75) 4) The parameter $\bar{w}$ used to define $\tilde{t}$ in Eq. (57) is further related to the dimensionless $\bar{V}_{\text{ext}}$, $\bar{\mu}_{\text{att}}$, $\bar{C}_m$, and $p_M/p_m$ in Eq. (33). 5) In between the limits $\tilde{t} \ll 1$ and $\tilde{t} \gg 1$ the behaviour of the exact solution Eq. (61) depends on a more complex combination of $\tilde{x}$ and $\tilde{t}$.

[23] Also: $\tilde{\text{Sh}} = \frac{\bar{L}_s}{2}\frac{t_D}{t_s}$ so that $\tilde{t} = \frac{\bar{L}_s^2}{8\bar{w}p_m}\frac{t_D}{t_s^2}t$ but we prefer to keep $\tilde{\text{Sh}}$ here.

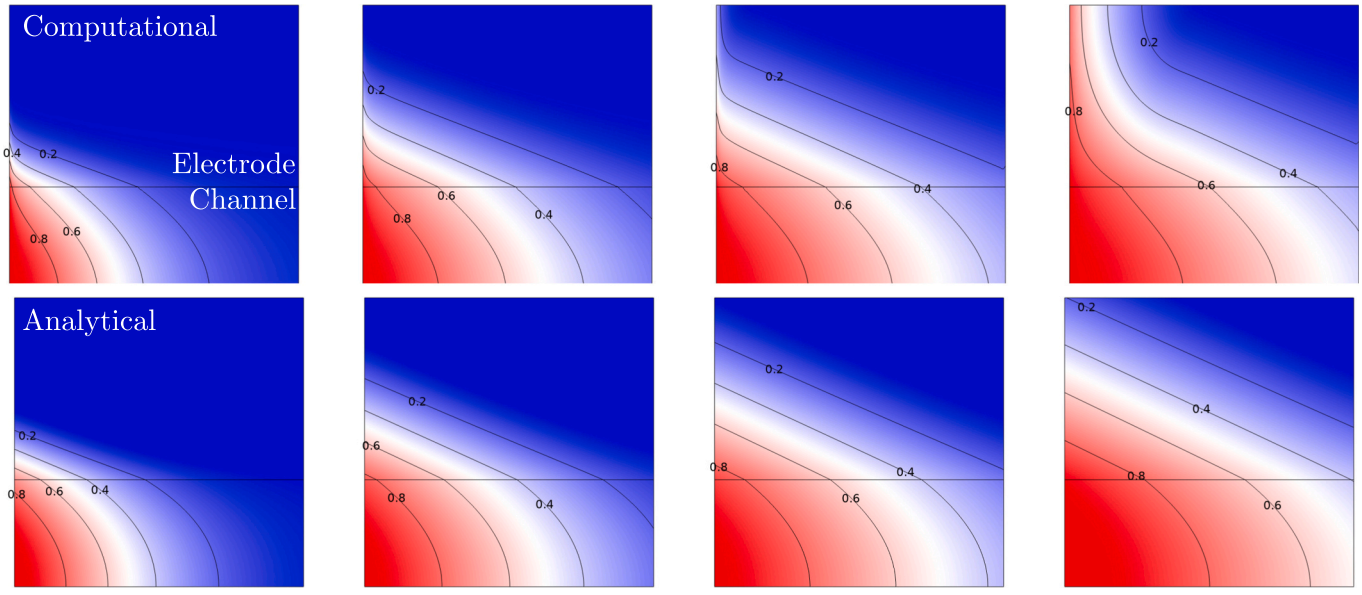


**Fig. 10.** Dimensionless concentration profiles $\bar{c}(x,y,t)$ for various dimensionless times using the parameters in Tables 1 and 2 at $\bar{V}_{ext} = 40$ (top) simulated in COMSOL; compared to (bottom) the analytical profile of Eq. (41) using Eqs. (74) and (75).

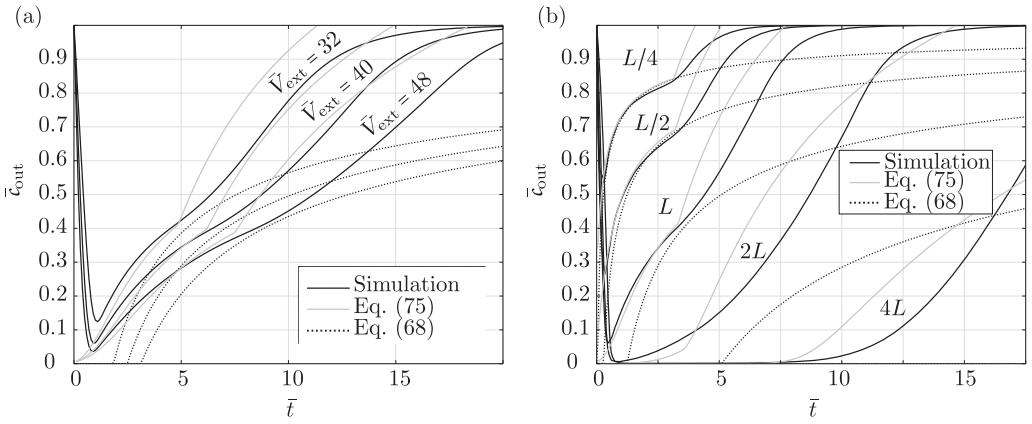


**Fig. 11.** Dimensionless cup-mixing concentration at the channel outlet, $\bar{c}_{out}$ given by the COMSOL simulation, compared with the analytical solution, including the charged approximation (Eq. (75)), and the approximate solution (Eq. (68)) using the parameters in Tables 1 and 2 at (a) $\bar{V}_{ext} = 32$, 40, and 48 and (b) for channel lengths $L/4$, $L/2$, $L$, $2L$ and $4L$. Eq. (75) gives an excellent match to the simulation for $t_D < t < t_c + t_D$ and approximately includes the effect of the electrode becoming locally fully charged for $t > t_c + t_D$. The time $\bar{t}_c + 1$ can be clearly seen by the trend change in the analytical solution.

### 7.1. Channel length L and charging time T

The dimensionless penetration depth $\tilde{\delta} = \sqrt{1 + 2\tilde{t}}$ will increase in time. As long as the channel length is larger than this depth, the outlet concentration will remain low relative to the inlet concentration. To maintain a low outlet concentration[24] throughout the charging phase, but not use more electrode area than strictly needed, we propose to use a channel length approximately equal to the penetration depth at the end of the charging phase. Note that in case $\tilde{T} \gg 1$ this will mean that initially, at the start of the charging phase, a large fraction of the electrode will be inactive, as illustrated in Fig. 7. However, this choice allows us to make no compromise and always ensure a high salt-rejection.

Additionally, to ensure that the electrode is not unnecessarily thick we will demand that at the end of the charging phase the electrode is fully charged at $x = 0$, so $\tilde{T} = \tilde{t}_c$.[25] Eq. (70), together with $\tilde{T} = \tilde{t}_c$ and $\tilde{L} = \tilde{\delta} = \sqrt{1 + 2\tilde{T}}$, gives

[24] For small times $\tilde{t} \ll 1$, inserting $\tilde{L} = 1$ in Eq. (65) gives $\bar{c} \approx 1/e \approx 0.37$. This is not particularly small, so that in this case, depending on the requirements, a slightly longer channel should be chosen. Doubling the channel length reduces the outlet concentration to a perhaps more acceptable $e^{-2} \approx 0.13$.

[25] Note that part of the electrode material near the outlet will remain underused in this case. Therefore, to save material, the electrode could be made thinner there. The analytical result for $\zeta(x,T)$ can be used to find the optimal shape. Alternatively, a single electrode may be shared between two counter-current flow-channels in a monopolar stack so that the electrode is used fully. To avoid advective cross-over, the hydraulic resistance of the electrodes should be sufficiently high in this case. In case it will not be strictly necessary to always maintain a low outlet concentration throughout the charging phase, for example when continuously recycling the salt solution, Eq. (71) may alternatively be used to relate $T$ and $L$, so that entire electrode is fully charged at the end of the charging phase.

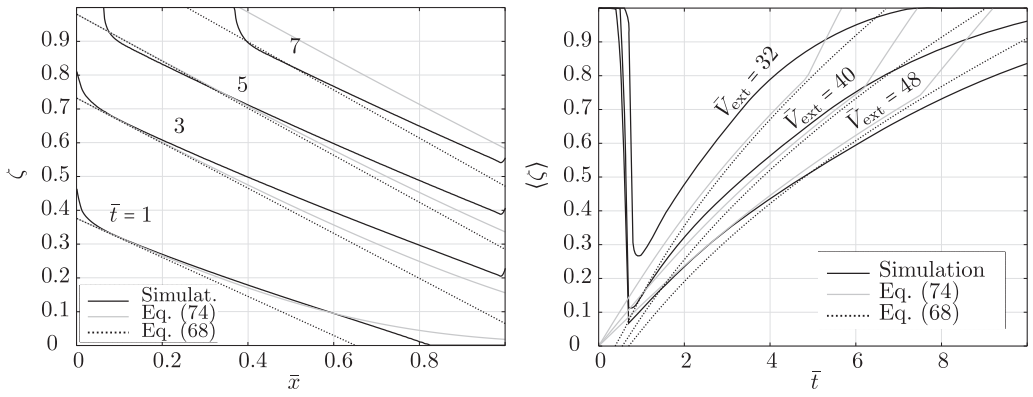


**Fig. 12.** (a) The dimensionless location $\zeta = \frac{y - L_s/2}{L_e}$ of the concentration shock in the electrode at $\bar{V}_{ext} = 40$ and (b) the $x$-averaged depth of the concentration shock in the electrode at $\bar{V}_{ext} = 34$, 40, and 48, given by the simulation (there where $\bar{c} = 0.05$), the analytical solution with the charged approximation (Eq. (74)), and the approximate solution (Eq. (68)). Shortly after the electrode becomes locally fully charged ($t > t_c$), the shock front begins to encroach more rapidly to account for the inability of the charged electrode in $x < x_c$ to adsorb salt.

$$\widetilde{T}_{opt} = \widetilde{Sh}(\widetilde{Sh}/2 + 1), \tag{78}$$

$$\widetilde{L}_{opt} = \widetilde{Sh} + 1. \tag{79}$$

Inserting dimensions gives[26]

$$T_{opt} = p_m \bar{w}\left(\frac{L_e^2}{D_e} + \frac{4L_s L_e}{Sh_s D}\right), \tag{81}$$

$$L_{opt} = \frac{UL_s L_e}{2D_e} + \frac{UL_s^2}{DSh_s}. \tag{82}$$

The first term in these expressions is the result for negligible spacer mass transfer resistance $\widetilde{Sh} \gg 1$ or $L_s \ll L_e \frac{Sh_s D}{2D_e}$. The final term dominates in case the mass transfer in the electrodes is negligible compared to that in the spacer.

### 7.2. Productivity

The productivity P [m/s] gives the volume of water desalinated per unit time, per unit geometrical frontal electrode area. This is a useful performance metric as it divides something desirable; the volume of treated water, by something that is undesirable due to the costs associated with it; electrode area. Inserting Eq. (82) gives in the productivity for an optimally long electrode as

$$P \equiv \frac{UL_s}{L} = \frac{1}{\frac{L_e}{2D_e} + \frac{L_s}{DSh_s}}. \tag{83}$$

The inverse of the productivity thus follows as the sum of the inverse of two mass transfer coefficients: $2D_e/L_e$ for the two electrodes and $DSh_s/L_s$ in the spacer. Somewhat counter-intuitively, a decrease in spacer thickness can thus lead to a higher productivity. Increasing the productivity, given the used constraints of Eq. (79), thus purely requires improving the mass transport. We note that increasing $Sh_s$, for example through fluidic dispersion in a porous spacer or by means of static mixers, has the same effect as decreasing the spacer thickness $L_s$. On the other hand, mass transport inside the electrodes can be improved with either thinner electrodes or with additional mixing by means of flow through the electrodes.

### 7.3. Electrode/spacer thickness

For a fully-developed laminar flow the planar Hagen-Poiseuille equation gives for the pressure drop

$$\Delta p = 12\mu \frac{U}{L_s^2} L. \tag{84}$$

A larger spacer thickness will allow processing more salt at the same velocity or pressure drop. However, a too large thickness can give additional mass transfer resistance as well as ohmic resistance. Several metrics related to energy efficiency can be devised, see Appendix F.5. Here we aim to minimize the dissipation per unit area with respect to the spacer distance. The dissipation per unit area due to pumping $UL_s\Delta p/(L\eta_p) = P\Delta p/\eta_p$ is given by the product of volumetric flow rate and pressure drop, divided the area and the pump efficiency $\eta_p$. The ohmic dissipation in the spacer per unit area, $jF\Delta\phi_{\Omega,s}$, is given by the product of the current density $jF$ and the average ohmic drop in the spacer $\Delta\phi_{\Omega,s}$. Using conservation of salt we find, in the case that all inlet salt is adsorbed, that the flux $j(z)$ is constant and equal to the channel-averaged flux $\langle j\rangle = UL_s c_0/L = Pc_0$. The concentration, and therefore the conductivity, will decrease along the channel away from the inlet. From the simulations, we find it to be a reasonable approximation to calculate the average ohmic dissipation using half the inlet conductivity. This gives for the dissipated power in the spacer per unit area [W/m$^2$]

$$P_{spacer} \approx (F\langle j\rangle)^2 \frac{L_s}{\kappa_0} + \frac{12\mu U^2}{\eta_p L_s} = P^2\left(FV_T c_0 \frac{L_s}{D} + \frac{12\mu L^2}{\eta_p L_s^3}\right), \tag{85}$$

where we used Eqs. (84) and (15) to give $\kappa_0 = \frac{2FD}{V_T} c_0$. Counter-intuitively, the ohmic losses increase with increasing $c_0$ because the current increases with increasing $c_0$.

The ratio of the spacer dissipation and the productivity $P_{spacer}/P$ gives the number of Joules dissipated in the spacer per cubic meter of water processed. Clearly, this is something one would want to minimize. The productivity P, on the other hand is something to be maximized. To take both of these desires into account we propose to maximize the ratio of these two metrics, or $P^2/P_{spacer}$. This will be equal to minimizing $P_{spacer}/P^2$, which is given by the expression between brackets in Eq. (85). Note that this is the first and only significant trade-off we make. In this minimization, we do not assume a fixed channel length $L$ but instead

[26] We are constrained by $T \gg L/U$ implied by Eq. (19), which is shown in Eq. (F.1) to guarantee a high flow-efficiency. Eq. (34) showed this to be satisfied when

$$\frac{L_s}{L_e} \ll \frac{p_m w}{c_0} \tag{80}$$

So, the higher the amount of salt $p_m w$ that can be stored per unit volume, relative to the inlet concentration $c_0$, the thicker the spacer can be made relative to the electrode. Inserting $T$ from Eq. (81) and $L/U$ from Eq. (82) shows that these optimal values roughly satisfy this constraint.

include its dependence on $L_s$ through Eq. (82). Inserting this relation and solving $\partial(P_{spacer}/P^2)/\partial L_s = 0$ gives after some algebra

$$\widetilde{\mathrm{Sh}}_{opt} \equiv \frac{\mathrm{Sh}_s D}{2D_e}\frac{L_e}{L_s} = \sqrt{1+\frac{U_{opt}^2}{U^2}}, \tag{86}$$

where

$$U_{opt} \equiv \sqrt{\frac{FV_T c_0 D\eta_p}{12\mu}}\mathrm{Sh}_s. \tag{87}$$

The optimal spacer to electrode mass transfer coefficient ratio is thus equal to one (when $U \gg U_{opt}^2$) or larger than one. So the mass transfer in the channel should be always at least as good as that in the electrode. Inserting Eq. (86) into Eq. (83) gives

$$P = \frac{D\mathrm{Sh}_s/L_s}{1+\sqrt{1+U_{opt}^2/U^2}}. \tag{88}$$

### 7.4. Optimal parameters

We here summarize the various formulas for optimal parameters derived above and insert typical values from Table 1. From Eq. (88) we find that when $U$ is at or above $U_{opt}$ the productivity is close to its maximum and can no longer be improved with increasing the velocity. There are however disadvantages to increasing the velocity more than needed, for example an increase in pressure drop. Therefore, we propose $U_{opt}$ as an optimal value. This gives a productivity that is less than 20 % below its maximum.

The spacer thickness then follows from the desired productivity P from Eq. (88) as

$$L_{s,opt} = \frac{D\mathrm{Sh}_s/P}{1+\sqrt{2}} \approx \frac{23\,\mathrm{mm}}{P[\mathrm{l/h/m^2}]}. \tag{89}$$

For the values in Table 1 used in our simulations and in the simulations and experiments of Ref. [27] the productivity is 12.6 l/h/m$^2$, see also Table 3. This gives an optimal spacer thickness of 1.85 mm, compared to the used 0.8 mm. Since the productivity is the volumetric flow rate of treated water per unit area, the choice for a desired productivity will typically depend on economical arguments related to the cost of materials and the value of desalinated water. For a more ambitious productivity the optimal spacer thickness can become very thin.

With $U = U_{opt}$, Eq. (86) shows that $\tilde{\mathrm{Sh}}_{opt} = \sqrt{2}$ so Eq. (86) gives

$$\frac{L_{e,opt}}{L_{s,opt}} = \frac{2\sqrt{2}D_e}{\mathrm{Sh}_s D} \approx 0.17, \tag{90}$$

in the final expression inserting the values from Table 1. The electrode should thus be substantially thinner than the spacer, to keep their mass transfer coefficients of similar size. Note that Eq. (90) combines with Eq. (34) to give $c_0 \lesssim p_m w$ providing a maximum inlet concentration for a given capacitance and voltage.

**Table 3**
Optimal geometrical and operational parameters for two different throughput productivities, the second 20 times larger than the first. They both correspond to $c_0 = 1$ mM and have the same velocity of $U_{opt} = 0.14$ m/s and pressure drop of $\Delta p_{opt} = 0.4$ bar. We used $D = 2D_e = 1.9{\cdot}10^{-9}$ m/s, $\mu = 1$ mPa s, $\mathrm{Sh}_s = 140/17$, $p_m = 0.3$, $w = 0.29$ M (from Eq. (33) with $C_m = 1.5{\cdot}10^8$ F/m$^3$ and $\bar{V} = 40$), $V_T = 25$ mV, and $\eta_p = 0.8$.

| $P = UL_s/L$: | 12.6 l/h/m$^2$ | 252 l/h/m$^2$ |
|---|---|---|
| $L_{s,opt}$ | 1.85 mm | 93 µm |
| $L_{e,opt}$ | 320 µm | 16 µm |
| $L_{opt}$ | 76 m | 19 cm |
| $T_{opt}$ | 6.2 h | 1 min |

Next, we turn to the optimal velocity which by Eq. (87) depends only on $c_0$, which in the below equations has units of mol/m$^3$ or mM

$$U_{opt} \approx 0.14\sqrt{c_0[\mathrm{mM}]}\,\mathrm{m/s}, \tag{91}$$

where we assumed a pump efficiency $\eta_p = 80$ %. So even for a low $c_0 = 1$ mM the optimal velocity is 0.14 m/s, which is several orders of magnitude higher than what is typically used. Correspondingly, with such high velocities the channels should be much longer. Eqs. (78) and (79) become, after inserting $U_{opt}$ from Eq. (87)

$$T_{opt} = 8\left(1+\sqrt{2}\right)\bar{w}p_m D_e\left(\frac{L_{s,opt}}{\mathrm{Sh}_s D}\right)^2 \approx 1.8\frac{(L_{s,opt}[\mathrm{mm}])^2}{c_0[\mathrm{mM}]}\mathrm{h}, \tag{92}$$

$$L_{opt} = \left(1+\sqrt{2}\right)L_{s,opt}^2\sqrt{\frac{FV_T c_0\eta_p}{12\mu D}} \approx 22(L_{s,opt}[\mathrm{mm}])^2\sqrt{c_0[\mathrm{mM}]}\mathrm{m}, \tag{93}$$

where we used a constant $w = 0.29$ M corresponding to the 1 V values in Tables 1 and 2 using $c_0 = 1$ mM.[27] With an optimal spacer thickness of 1.85 mm and $c_0 = 1$ mM, this gives a channel length of 76 m and a charging time of 6.2 h. Such long channels may be fabricated using serpentine flow fields. We note that higher capacitance electrodes with a higher $\bar{w}$ give a longer charging time $T_{opt}$, increasing the flow efficiency of Eq. (F.1). Unless a higher capacitance comes at the expense of for example a lower macro porosity, the effect seems to be primarily beneficial.

Inserting $U_{opt}$, $L_{opt}$, and Eq. (90) into Eq. (84) gives

$$\Delta p_{opt} = \left(1+\sqrt{2}\right)FV_T c_0\eta_p\mathrm{Sh}_s \approx 0.4(c_0[\mathrm{mM}])\mathrm{bar}, \tag{94}$$

resulting in a substantial pressure drop of 0.4 bar for $c_0 = 1$ mM and a high 7.7 bar for the $c_0 = 20$ mM used in the experiments of Ref. [27]. The optimal processing of more concentrated brines with CDI thus requires rather high pressure equipment. Practical considerations like the maximum head of a pump, or the maximum pressure allowed by the cells to avoid leakages will therefore determine the maximum salt concentration that can be optimally processed.

In Table 3 we compare the optimal values for two different cases, one with the same productivity of 12.6 as used in the simulations and Ref. [27], and a more ambitious case with a twenty times higher productivity. This is an extremely high productivity, an order of magnitude larger than what is typically achieved in CDI or similar techniques [25,45].

## 8. Conclusion and discussion

We provided a comprehensive mathematical analysis of flow-by capacitive deionization in the mass-transport limited regime. The various conditions on time-scales, Eq. (19), electrode capacitance, Eqs. (31) and (34), and geometry, Eq. (20), are often satisfied for the concentrations and potentials used in CDI. For a modified Donnan model with unit charge efficiency, we found an exact expression for the micropore potential drop: Eq. (26). A simplified expression, Eq. (49), was obtained for the ohmic drop.

The model equations were reduced to two dimensionless coupled partial differential equations, Eqs. (52) and (53), for which we were able to find an exact analytical solution, Eq. (61), and excellent approximations: Eqs. (66) and (68). The analytical solution was verified against a numerical solution and successfully compared to COMSOL simulations using a comprehensive 2D transient model.

Using the approximate solutions we found expressions for the

[27] This value is obtained from Eq. (33) and weakly depend on the concentration. For the twenty times higher $c_0 = 20$ mM used in the simulations it gives $w \approx 0.26$ M and the 1.8 in Eq. (92) changes to 1.6.

optimal channel length and charging time that maintains a low outlet concentration up to the point the electrode is fully charged near the inlet. In order to find optimal values for the spacer and electrode thickness, we assumed a desired volumetric flow rate per unit area, or productivity. In Eq. (83) we find that the inverse of the productivity is given by the sum of the inverse of the channel and electrode mass transfer coefficients, the expected equivalent circuit of two mass transfer resistances in series. The ratio of the productivity and spacer energy dissipation per unit volume of treated water is maximized, resulting in an optimal electrode to spacer thickness ratio of around 0.17, viz. Eq. (90). In turn, the optimal spacer thickness is inversely proportional to the desired productivity viz. Eq. (89). The resulting pressure drop of these optimal conditions is found to be around 0.4 bar per 1 mM of inlet concentration. Therefore, operation under these optimal conditions will only be feasible at relatively low concentration. We found that with the proper proposed design parameters it should be possible to process a very high 250 l/h/m$^2$ of 1 mM brackish water in a 0.2 m long channel with a charging time of 1 min. This analysis gives the thorough quantitative understanding necessary to show the direction in which CDI cells should be designed to be as productive and efficient as possible.

## CRediT authorship contribution statement

**J.W. Haverkort:** Conceptualization, Formal analysis, Investigation, Methodology, Software, Supervision, Validation, Visualization, Writing – original draft. **B. Sanderse:** Software, Validation, Writing – review & editing. **J.T. Padding:** Supervision, Writing – review & editing. **J.W. Blake:** Formal analysis, Investigation, Software, Visualization, Writing – review & editing.

## Declaration of competing interest

The authors declare that they have no known competing financial interests or personal relationships that could have appeared to influence the work reported in this paper.

## Data availability

Data will be made available on request.

## Acknowledgement

We are grateful for the help received from W.T. van Horssen with the derivation in Appendix B. This work is part of the research programme Electrons to Chemical Bonds (E2CB) with project number P17-09-01, which is (partly) financed by the Dutch Research Council (NWO).

## Appendix A. Lambert W approximation

The Lambert W function, referred to as ProductLog in Mathematica, is a special function defined by Eq. (27). We are interested here in positive arguments, giving the zeroth branch, sometimes denoted with $W_0$. We found that this function can be approximated with a relative error always below 3% using

$$W(x) \approx \begin{cases} \dfrac{x}{1+0.8x^{0.8}} & x < 2.3 \\ \ln\dfrac{kx}{\ln x} & x \geq 2.3, \end{cases} \tag{A.1}$$

where

$$k(x) \approx \frac{1+(\ln\sqrt{x})^{0.77}}{(\ln x)^{-1}+(\ln\sqrt{x})^{0.77}} \quad \text{for } x \geq 2.3. \tag{A.2}$$

The function $k$ varies only weakly between $1.26 \lesssim k \lesssim 1.39$ for $5 \leq x \leq 10^4$ and tends to unity in the limit of $x \to \infty$.

In Eq. (26) we have $x = \frac{\bar{c}e^{\widetilde{V}/2}}{2\bar{C}_m}$. *Assuming* $x \gtrsim 2.3$, or using the definition in Eq. (25)

$$\frac{\Delta\widetilde{V}}{2} \gtrsim \ln\left(\frac{4.6\bar{C}_m}{\bar{c}}\right), \tag{A.3}$$

we can use the second approximation in Eq. (A.1) with $k \approx 1.3$ approximately constant, to approximate Eq. (26) as

$$\Delta\bar{\phi}_m = \frac{\bar{w}_m}{\bar{C}_m} \approx \frac{\widetilde{V}}{2} - \ln\left(\frac{2\bar{C}_m}{k\bar{c}}\left[\frac{\widetilde{V}}{2}+\ln\left(\frac{\bar{c}}{2\bar{C}_m}\right)\right]\right). \tag{A.4}$$

From this we calculate $\Delta\bar{\phi}_D = \frac{\bar{V}_{ext}}{2} - \Delta\bar{\phi}_\Omega - \Delta\bar{\phi}_m$ to be given by

$$\Delta\bar{\phi}_D = \ln\left(\frac{2\bar{C}_m}{k\bar{c}}\left[\frac{\widetilde{V}}{2}+\ln\left(\frac{\bar{c}}{2\bar{C}_m}\right)\right]\right) - \bar{\mu}_{att}, \tag{A.5}$$

so that with $\bar{w}_m \approx \frac{\bar{c}}{2}e^{\Delta\bar{\phi}_D+\bar{\mu}_{att}}$

$$\bar{w}_m \approx \frac{\bar{C}_m}{k}\left[\frac{\widetilde{V}}{2}+\ln\left(\frac{\bar{c}}{2\bar{C}_m}\right)\right]. \tag{A.6}$$

Interestingly, this approximation $W(x) \approx \frac{\ln x}{k}$, differs from that of Eqs. (A.1) and (A.4). Without the approximation of Eq. (A.1), Eq. (A.6) would read

$\bar{w}_m = \frac{\tilde{c}e^{\bar{\mu}_{att}}}{2} e^{\bar{V}_{ext}/2 - W(x)}$ which with $W(x)e^{W(x)} = x$ would be equal to the solution of Eq. (26). However, the approximation of Eq. (A.1) does not exactly satisfy this relation, so that a small difference arises between these expressions. However, as long as $x \geq 2.3$ the difference is small. The expression of Eq. (A.6) has the advantage of being slightly simpler, while the expression of Eq. (A.4) is much less sensitive to the exact value of $k$ used and is accurate for large arguments using the simple constant value $k = 1$, which is therefore used in the second approximation of Eq. (28).

Eq. (A.5) gives with some algebra for $\bar{c} = 2\bar{w}e^{-\bar{\mu}_{att} - \Delta\bar{\phi}_D}$,

$$\bar{c} \approx 2\bar{C}_m e^{\frac{k\bar{w}_m}{\bar{C}_m} - \frac{\bar{V}}{2}}. \tag{A.7}$$

## Appendix B. Exact solution derivation

Here we derive an exact solution to Eqs. (52)-(53), which satisfy the following conservation equation

$$\frac{\partial c}{\partial \tilde{x}} + \frac{\partial \tilde{\zeta}}{\partial \tilde{t}} = 0, \tag{B.1}$$

where, from Eq. (53),

$$c = (1 + \tilde{\zeta}) \frac{\partial \tilde{\zeta}}{\partial \tilde{t}}. \tag{B.2}$$

Inserting this into Eq. (B.1) gives

$$\frac{\partial \tilde{\zeta}}{\partial \tilde{x}} \frac{\partial \tilde{\zeta}}{\partial \tilde{t}} + (1 + \tilde{\zeta}) \frac{\partial^2 \tilde{\zeta}}{\partial \tilde{t} \partial \tilde{x}} + \frac{\partial \tilde{\zeta}}{\partial \tilde{t}} = 0, \tag{B.3}$$

which can be written as

$$\frac{\partial}{\partial \tilde{t}} \left[ (1 + \tilde{\zeta}) \frac{\partial \tilde{\zeta}}{\partial \tilde{x}} \right] + \frac{\partial \tilde{\zeta}}{\partial \tilde{t}} = 0. \tag{B.4}$$

This can be integrated with respect to $\tilde{t}$ to give

$$(1 + \tilde{\zeta}) \frac{\partial \tilde{\zeta}}{\partial \tilde{x}} + \tilde{\zeta} = \tilde{\zeta}_0, \tag{B.5}$$

where $\tilde{\zeta}_0$ is the solution at $\tilde{t} = 0$, since for our initial conditions $\frac{\partial \tilde{\zeta}}{\partial \tilde{x}} = 0$ at $\tilde{t} = 0$. Equation (B.5) can be classified as particular case of an Abel equation of the second kind. We can solve it, for example using the method of characteristics, to give [28]

$$\frac{\tilde{\zeta} - \tilde{\zeta}_0}{1 + \tilde{\zeta}_0} = W\left( \frac{e^{f(\tilde{t}) - \frac{\tilde{x}}{1 + \tilde{\zeta}_0}}}{1 + \tilde{\zeta}_0} \right). \tag{B.6}$$

Inserting into Eq. (B.2) and solving the boundary condition $c(\tilde{x} = 0, \tilde{t}) = 1$ gives

$$f(t) = \hat{t} + \ln(\hat{t}(1 + \tilde{\zeta}_0)), \tag{B.7}$$

where $\hat{t}$ is given by

$$\hat{t} \equiv \sqrt{1 + \frac{2\tilde{t}}{(1 + \tilde{\zeta}_0)^2}} - 1 \approx \begin{cases} \frac{\tilde{t}}{(1 + \tilde{\zeta}_0)^2} & \ll 1, \\ \frac{\sqrt{2\tilde{t}}}{1 + \tilde{\zeta}_0} & \gg 1. \end{cases} \tag{B.8}$$

Eq. (B.7) satisfies $(1 + \tilde{\zeta}_0)^2 \frac{df}{dt} = \frac{1}{t}$. Eq. (B.2) gives $c = (\tilde{\zeta} - \tilde{\zeta}_0) \frac{df}{dt}$ so $c = \frac{1}{t} W\left( \frac{e^{f(\tilde{t}) - \frac{\tilde{x}}{1 + \tilde{\zeta}_0}}}{1 + \tilde{\zeta}_0} \right)$ and from Eq. (B.6) we find $\frac{\tilde{\zeta} - \tilde{\zeta}_0}{1 + \tilde{\zeta}_0} = \hat{t}c$.

## Appendix C. Numerical solution of the simplified model

Conveniently, the system of equations (52)-(53) with conditions (58) and (59) has no free parameters so that it has a single unique solution that we have to obtain only once. The same solution can be used for any inlet concentration, cell voltage, electrode capacitance, etc. by converting back the dimensionless variables of Eqs. (55)-(57) to dimensional variables. When the numerical solution is obtained once for a large enough range of $\tilde{t}$ and $\tilde{x}$,

[28] We may introduce a new variable $s$ in terms of which $\frac{d\tilde{\zeta}}{ds} = 1 + \tilde{\zeta}$ so that $\frac{d\tilde{\zeta}}{ds} = \tilde{\zeta}_0 - \tilde{\zeta}$. This can be solved to give $\tilde{\zeta} = \tilde{\zeta}_0 + Ce^{-s}$ so that $\tilde{x}(s) = s(1 + \tilde{\zeta}_0) - ke^{-s} + C_2$. Solving for $s$ and inserting into $\tilde{\zeta} = \tilde{\zeta}_0 + Ce^{-s}$ gives the solution.

the solution for any channel length and charging cycle duration can be obtained from it.

The coupled partial differential equations Eqs. (52) and (53) will here be solved using a finite difference solution. We introduce a computational grid consisting of $N_x$ nodes located at $\tilde{x}_i = i\Delta\tilde{x}$, $i = 1 \ldots N_x$, and $\Delta\tilde{x} = \tilde{x}_{N_x}/N_x$. On this grid we have the approximations $\bar{c}_{h,i}(\tilde{t}) \approx \bar{c}(\tilde{x}_i, \tilde{t})$ and $\tilde{\zeta}_{h,i}(t) \approx \tilde{\zeta}(\tilde{x}_i, \tilde{t})$. The first order derivative in (52) is then discretized by the central difference approximation

$$\frac{\partial \bar{c}}{\partial \tilde{x}} \approx \frac{\bar{c}_{h,i+1} - \bar{c}_{h,i-1}}{2\Delta\tilde{x}}. \tag{C.1}$$

After spatial discretization, the system (52)-(53) can thus be written as

$$D_h \bar{c}_h(\tilde{t}) = -f_h(\bar{c}_h(\tilde{t}), \tilde{\zeta}_h(\tilde{t})), \tag{C.2}$$

$$\dot{\tilde{\zeta}}_h(\tilde{t}) = f_h(\bar{c}_h(\tilde{t}), \tilde{\zeta}_h(\tilde{t})), \tag{C.3}$$

where $D_h$ is the $N_x \times N_x$ matrix that represents the central difference approximation (C.1). This semi-discrete system can be viewed as consisting of one evolution equation, (C.3), and a constraint (C.2). This constraint introduces so-called stiffness in the problem, so that we propose to use the implicit BDF2 time integration method and to handle the constraint (C.2) fully implicitly in time. This leads to the following system of equations that is solved at each time step:

$$D_h \bar{c}_h^{n+1} = -f_h(\bar{c}_h^{n+1}, \tilde{\zeta}_h^{n+1}), \tag{C.4}$$

$$\frac{\frac{3}{2}\tilde{\zeta}_h^{n+1} - 2\tilde{\zeta}_h^{n} + \frac{1}{2}\tilde{\zeta}_h^{n-1}}{\Delta\tilde{t}} = f_h(\bar{c}_h^{n+1}, \tilde{\zeta}_h^{n+1}). \tag{C.5}$$

Here $\bar{c}_{h,i}^{n+1}$ is the approximation to $\bar{c}(\tilde{x}_i, \tilde{t}^n)$. This is a coupled system of nonlinear equations that can be efficiently solved with Newton's method. The required Jacobian matrices $\frac{\partial f_h}{\partial c_h}$ and $\frac{\partial f_h}{\partial \tilde{\zeta}_h}$ can be computed analytically. The overall accuracy of the discretization method is second order in space and time. The used Matlab code will be free to use as a supporting information file. The result for four different times $\tilde{t} = 0.1$, 1, 10, and 100 is shown in Fig. C.13. The agreement with the analytical results gives confidence in the correctness of the analytical solution as well as the numerical implementation.

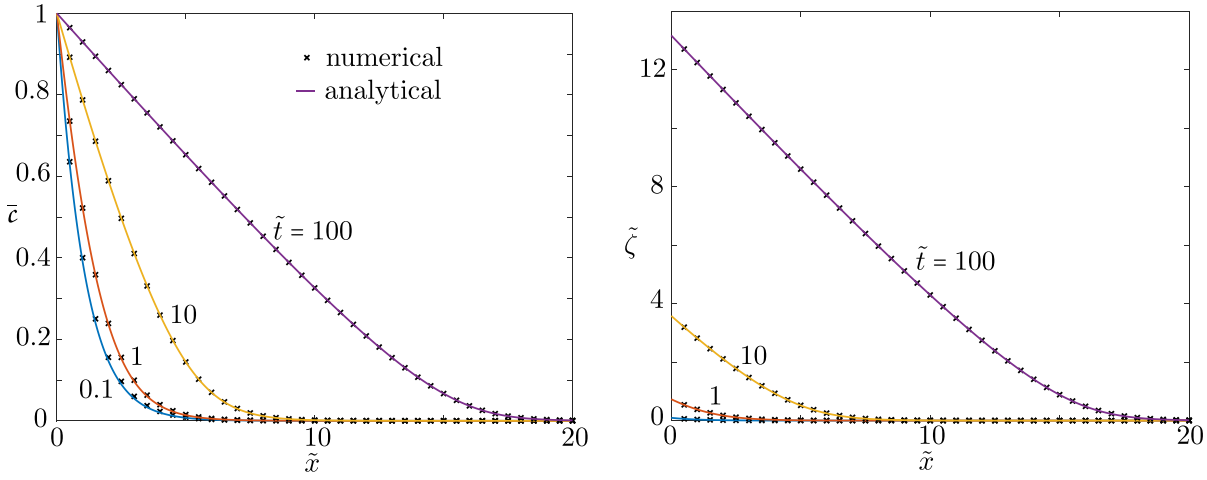


**Fig. C.13.** The dimensionless concentration $\bar{c}$ and mass-transfer ratio $\tilde{\zeta}$ obtained from solving Eqs. (C.4) and (C.5) (crosses) and the exact solution from Eq. (61) (coloured solid lines) for $\tilde{t} = 0.1, 1, 10, 100$.

## Appendix D. Approximate solutions

For $\tilde{\zeta} \ll 1$ the mass transfer resistance in the electrodes is negligible compared to that in the channel. Integrating Eq. (52) with $\tilde{\zeta} = 0$ gives

$$\bar{c} = \mathrm{e}^{-\tilde{x}}. \tag{D.1}$$

This time-independence approximation is only a good approximation for small times $\tilde{t} \ll 1$. For larger times we find the following expressions to be reasonably good approximations

$$\tilde{t} \lesssim \mathcal{O}(1), \tag{D.2}$$

$$\tilde{t} \lesssim \mathcal{O}(10), \tag{D.3}$$

$$\tilde{t} \sim \mathcal{O}(10^2). \tag{D.4}$$

These approximations are compared with the numerical solution in Fig. D.14 and agree very well, except for very low concentrations. Similarly, another insertion works better when $\tilde{t} \sim \mathcal{O}(10^3)$.

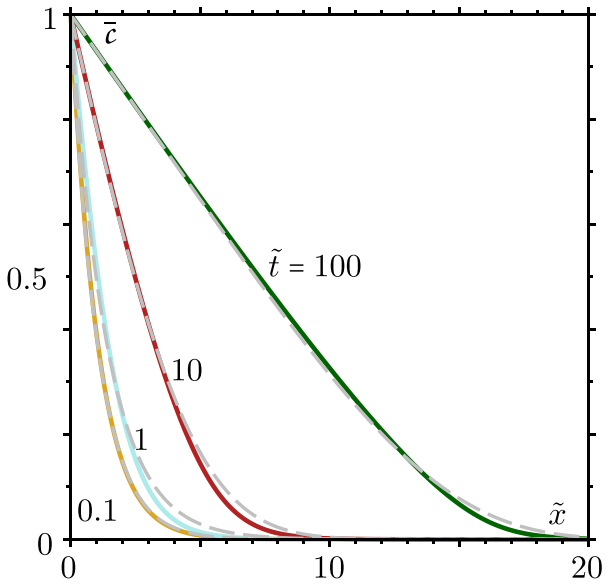


**Fig. D.14.** The exact analytical solution (solid curves) for the dimensionless concentration $\bar{c}$ of Eq. (63) is compared with the approximations (grey dashed lines) of Eqs. (66) ($\tilde{t} = 0.1$), (116) ($\tilde{t} = 1$), (117) ($\tilde{t} = 10$), (118) ($\tilde{t} = 10^2$)

## Appendix E. Time lag

The diffusion of salt into the electrode will not suddenly stop when the electrode is fully charged. Ions will no longer appreciable enter the *micro*pores, but the concentration in the *macro*pores is still smaller than that in the channel. Therefore, the diffusion of salt into the electrode will continue over a timescale of the order of the diffusion time $t_D = L_e^2/D_e$ or $\tilde{t}_D = \tilde{\mathrm{Sh}}^2/p_m\bar{w}$. However, Fig. E.15 shows that the diffusion of salt into the charged electrode continues for much longer. The reason is that as the current density decreases, the total ohmic drop reduces, increasing $\bar{w}$. A lower-estimate for the associated time-lag $t_{lag}$ is obtained by multiplying the initial superficial diffusion flux $D_e c_0 p_m/L_e$ with the electrode area $A$ and $t_{lag}$ to obtain the number of moles of salt added and equate this to to the number of moles $p_M A L_e c_0/2$ to be added to the macropores and $(\bar{w}_{max} - \bar{w}_0 - \bar{w})c_0 A L_e p_m$ to be added to the micropores to give

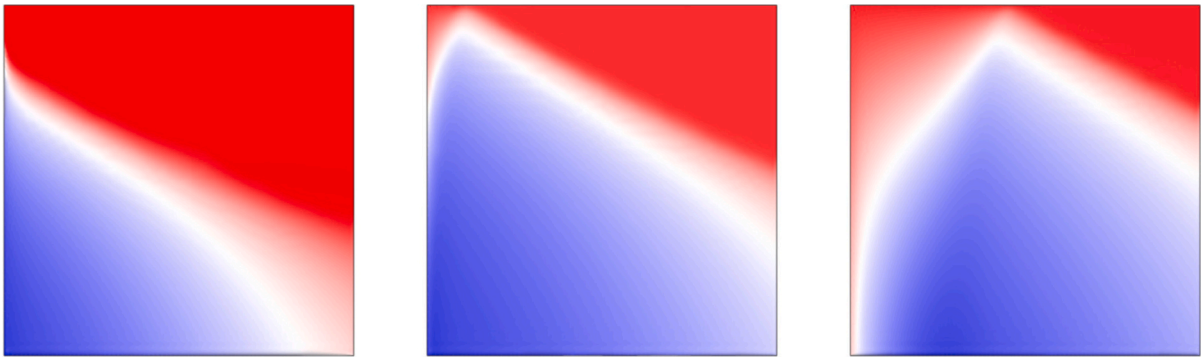


**Fig. E.15.** Simulated dimensionless macropore concentration gradient in the $y$-direction, $\frac{\partial \bar{c}}{\partial \bar{y}}$, inside the porous electrode, using the parameters in Tables 0 and 1 for $\bar{V}_{ext} = 40$. While the shock reaches the electrode edge around $\bar{t} \approx 4$, this is still only just beginning to have an effect on the flux at the spacer-electrode boundary at $\bar{t} = 7$. This is in part due to the diffusion time to fill the macropores, but additional adsorption capacity in the micro-pores is also freed up as the current density and therefore the ohmic drop decreases.

$$\bar{t}_{lag} \approx \frac{p_M}{2} + (\bar{w}_{max} - \bar{w}_0 - \bar{w})p_m \approx \frac{p_M + 0.87\bar{C}_m p_m}{2}, \tag{E.1}$$

where in the second expression we used the approximation of Eq. (32) to give $\bar{w}_{max} - \bar{w} \approx 0.87\bar{C}_m\Delta\bar{\phi}_\Omega/2$ and we neglected the second term in Eq. (49) assuming $\frac{\mathrm{Sh}_s}{1+\tilde{\zeta}} \ll 1$ so that $\Delta\bar{\phi}_\Omega \sim 1$. For the numbers in Table 1 this gives $\bar{t}_{lag} \approx 0.3$. This is an order of magnitude smaller than the time between the

arrival of the shock at the back of the electrode and the vanishing of the flux near the inlet in Fig. E.15. In part this is because the flux will decrease in time and only when it has decreased to zero does the ohmic drop vanish and can the additional micropore capacity be used. However, it is also clear, from e.g. Fig. 4, that the adsorption region is in actuality much more spread out than in our model. As a result, the shock arrives earlier than we predict and more additional micropore capacity than we predict will become available as the potential equilibrates. To take into account the effects of a more spread-out adsorption zone will require further investigation beyond the scope of this work.

After the time-lag, the diffusion into the electrode ceases locally and only then the average channel concentration profile will be impacted by the electrode being fully charged. Next, it takes roughly another transit time $x/U$ before this channel change is noticed further downstream, but in the present approximation we will not take this into account. We therefore modify Eq. (71) to $\tilde{x}_C \equiv \tilde{x}_c(\widehat{t}_C)$ or

$$\widetilde{x}_C = \widehat{t}_C - \widetilde{\mathrm{Sh}} + \ln\left(\frac{\widehat{t}_C}{\widetilde{\mathrm{Sh}}}\right), \tag{E.2}$$

where $\widehat{t}_C = \sqrt{1+2(\tilde{t}-\tilde{t}_{\mathrm{lag}})} - 1$ includes the time-lag. While $\tilde{x}_c$ gives the approximation location at which the electrode is fully charged, the position $\tilde{x}_C$ will roughly indicate the location at which the concentration profile will be impacted. Further downstream the electrode will not be fully charged so the desalination can continue.

## Appendix F. Metrics

Many different metrics for CDI exist in the literature. A useful feature of an analytical model is that these metrics can be evaluated analytically as well, providing 'structure-property' relations linking design parameters to performance. In this way, the cell geometry and operational conditions can be chosen in such a way that they maximize the desired performance metric.

### F.1. Charge efficiencies

Several commonly used measures of efficiency can be readily evaluated on the basis of our simplifying assumptions and conditions:

- The Coulombic efficiency $\lambda_c$ is the instantaneous ratio of electronic current and the rate of ion charge adsorption.[29] Since no leakage currents [51], for example due to water splitting or other side-reactions, have been included in the present model, we have a Coulombic efficiency $\lambda_c = 1$.
- The flow efficiency $\Lambda_{\mathrm{flow}}$ [24,31] quantifies the inefficiency associated with the finite volume of the spacer: during the first transit time $t_U$, the residence time is not as long as for newly entering water, resulting in poorer desalination. With $T$ the charging time, the flow efficiency can be approximated by [31]

$$\Lambda_{\mathrm{flow}} \approx 1 - t_U/2T. \tag{F.1}$$

Our model is only valid for times $t \gtrsim t_U$, see Section 2.3. Therefore, we typically consider $T \gg t_U$ so that $\Lambda_{\mathrm{flow}} \approx 1$.

- The differential charge efficiency $\lambda = \tanh\bar{\phi}_D$ is assumed to be approximately 1, see Eq. (22). Therefore, the equilibrium charge efficiency $\Lambda = \tanh(\bar{\phi}_D/2)$, see footnote 6, is also close to 1. The actual *dynamic* charge efficiency $\lambda\lambda_c\Lambda_{\mathrm{flow}} \approx 1$ that can be measured over a cycle [65] can in general differ from this equilibrium value [24].

### F.2. Salt rejection (SR)

The time-average of the relative concentration reduction $\frac{c_0 - c_{\mathrm{out}}}{c_0}$ during a cycle is called the *salt rejection* [38] SR, or salt-removal efficiency [62]. The analytical solution of Eq. (63) cannot be exactly integrated with respect to time. Therefore, we consider here the linear approximation of Eq. (68) which gives[30]

$$\mathrm{SR} \equiv \frac{1}{T}\int_0^T (1-\bar{c}_{\mathrm{out}})\,dt \approx 1 - \frac{\max\left(0, \sqrt{1+2\tilde{T}} - \tilde{L}\right)^2}{2\tilde{T}}. \tag{F.2}$$

$$\langle j \rangle = \frac{UL_s}{L}(c_0 - c_{\mathrm{out}}) \approx \frac{c_0 U L_s}{L}\min\left(1, \tilde{L}/\tilde{\delta}\right),$$

To obtain a high salt rejection close to SR=1 thus requires $\tilde{L}^2 > 1 + 2\tilde{T}$. This shows that the channel length has to be sufficiently high compared to the used flowrate, in order to store all the salt. Much larger will not be necessary, leading to the optimal channel length expression of Eq. (82).

[29] Sometimes it is defined on the basis of a full cycle in which $\lambda_c = 1$ corresponds to the electronic charge exchanged with the cell during charging equalling that during discharging [25].

[30] This requires splitting the integral into a range from a dimensionless $\tilde{t} = 0$ to $\frac{\tilde{L}^2-1}{2}$ during which the integrand is approximately 1 and the remaining part up to $\tilde{T}$. When $\tilde{L} < \sqrt{1+2\tilde{T}}$ and $\tilde{T} \gg 1$ we can alternatively write $\mathrm{SR} \approx 1 - \left(\frac{\tilde{L}}{\sqrt{2\tilde{T}}} - 1\right)^2 \approx \frac{2\tilde{L}}{\sqrt{2\tilde{T}}} - \frac{\tilde{L}^2}{2\tilde{T}}$.

### F.3. Throughput productivity (P)

A primary performance metric is the *(throughput) productivity* [m/s], the volume treated per unit geometrical electrode area and time, given by[31]

$$\mathrm{P} = \frac{L_\mathrm{s}}{L} U. \tag{F.4}$$

Note that a large spacer thickness $L_\mathrm{s}$ increases the productivity and decreases the pressure losses, but increases the ohmic losses. Therefore, an optimum has to be found here by invoking a combined productivity-energy metric.

A derived productivity metric is the Average Salt Adsorption Rate ASAR [mol/m$^2$/s][32]:

$$\mathrm{ASAR} = c_0 \mathrm{SR} \times \mathrm{P}. \tag{F.5}$$

This metric gives the number of moles of salt removed from the channel per unit area per discharge time. It is therefore equal to the time and space-average current density divided by $F$.

Another derived metric, the *salt adsorption capacity*, defined as the mass of adsorbed salt over a cycle divided by the combined electrode mass, is given by[33]

$$\mathrm{SAC} = \frac{MT}{2\rho_\mathrm{e} L_\mathrm{e}} \times \mathrm{ASAR}, \tag{F.7}$$

where $\rho_\mathrm{e}$ is the effective electrode density and $M$ the salt molarity [kg/mol].

### F.4. Current efficiency

Not all of the current is used for desalination. Salt adsorbed and removed from the inlet stream are not the same since some salt may be in the channel or micropores. The current efficiency CE is defined as the ratio of the ion charge removed from the channel and that passed by the current over a cycle [31].

Integrating Eq. (37) gives for the instantaneous space-averaged flux $\langle j \rangle \equiv \frac{1}{L}\int_0^L j dx$ [mol/m$^2$/s]

$$\mathrm{SEC} = \frac{IV_\mathrm{ext}T + \mathcal{V}\Delta p/\eta_\mathrm{pump}}{\mathcal{V}} = FV_\mathrm{ext}\Delta c + \frac{\Delta p}{\eta_\mathrm{pump}}, \tag{F.8}$$

where in the final expression we inserted Eq. (68). Note that this is an average over the entire channel length: the local flux in the region from $\tilde{x} = 0$ to $\tilde{x} = \tilde{\delta}$ is constant in the linear approximation of Eq. (68) and will be a factor $\tilde{L}/\tilde{\delta}$ higher when $\tilde{\delta} < \tilde{L}$. Integrating also over time gives for the time-and-space-averaged flux

$$\langle\langle j \rangle\rangle \equiv \frac{1}{T}\int_0^T \langle j \rangle dt = c_0 \frac{UL_\mathrm{s}}{L} \times \mathrm{SR} = \mathrm{ASAR}. \tag{F.9}$$

Since we assume a 100 % charge efficiency, this is also the salt-removal flux $J_\mathrm{salt}$. An additional amount of salt $2w_0 p_\mathrm{m} L_\mathrm{e}$ [mol/m$^2$] is initially transported in the $RC$-time, where $w_0 = c_0 \mathrm{e}^{\bar{\mu}_\mathrm{att}}$ is given by Eq. (30). Therefore, considering only the charging phase, the current efficiency $\mathrm{CE} \equiv \frac{\langle\langle j \rangle\rangle T}{\langle\langle j \rangle\rangle T + 2w_0 p_\mathrm{m} L_\mathrm{e}}$ reads with Eqs. (F.9):

$$\mathrm{CE} = \frac{1}{1 + \frac{2w_0 p_\mathrm{m} L_\mathrm{e}/T}{\mathrm{ASAR}}}. \tag{F.10}$$

here $2w_0 p_\mathrm{m} L_\mathrm{e}$ represents the number of moles of salt present in the micropores initially per unit area. We see from Eq. (F.10) that the goal of a high salt rejection and productivity, as quantified by ASAR, conveniently aligns with a high current efficiency. A longer charging time $T$ also helps to increase the current efficiency.

[31] With $L_z$ the thickness in the direction normal to the flow and the current, the volume of water treated over a discharge time $T$ is given by $\mathscr{V} = L_\mathrm{s} L_z U T$. With $A = L_z L$ the geometrical electrode area $A$, we have

$$\frac{\mathscr{V}}{A} = UT\frac{L_\mathrm{s}}{L}. \tag{F.3}$$

Usually the productivity is defined by dividing by the whole cycle time, but since we only consider the charging phase we use $T$ instead. Inserting Eq. (F.3) into $\mathrm{P} = \frac{\mathscr{V}}{AT}$ gives Eq. (F.4).

[32] Sometimes the term Average Salt Removal Rate (ASRR) is used to account for other ways of removal than adsorption [62]. Sometimes, instead of $U$ the volumetric flow rate of treated water is divided by the electrode mass rather than electrode area. [25].

[33] The product $MT \times$ ASAR gives the mass of adsorbed salt per unit area. The mass of the two electrodes, per unit area is $2\rho_\mathrm{e} L_\mathrm{e}$. The *maximum* or equilibrium salt adsorption capacity is the maximum amount of salt that can be adsorbed per unit electrode mass and is an important parameter for the comparison of different electrodes [56]. It is obtained by multiplying the maximum micropore salt concentration $2w_\mathrm{max}$ with the micropore volume $2p_\mathrm{m}V$ and dividing by the combined electrode mass. Sometimes also the electrode volume $V$ is used, which then gives in [mol/m$^3$]$\mathrm{mSAC} = 2w_\mathrm{max} p_\mathrm{m} \approx \frac{C_\mathrm{m} p_\mathrm{m}}{kF}\left(\frac{V_\mathrm{ext}}{2} + \mu_\mathrm{att} + V_T \ln\left(\frac{cF}{V_T C_\mathrm{m}}\right)\right)$, (F.6)where in the second approximation we used Eq. (32) and re-inserted dimensions. A value of $k \approx 1.15$ gives a reasonable approximation. This shows how this metric increases offset-linearly as a function of $V_\mathrm{ext}$ and sub-linearly as a function of $C_\mathrm{m}$ in our model.

### F.5. Energy

#### F.5.1. Specific energy consumption (SEC)

The energy consumption during the charging phase consist of direct electrical energy and pumping energy. The former is given by the product of applied voltage and current times charging time, while the latter is often neglected [62] and is given by multiplying the pressure drop $\Delta p$ with the flowed volume $\mathscr{V} = L_s L_z U T$ and dividing by the energy efficiency $\eta_{\text{pump}}$ of the pump. The specific energy consumption, in desalination generally is reported per unit volume water produced. In CDI it is typically rather per kg or mol of salt removed [58]. The *volumetric or specific energy consumption* SEC [J/m$^3$], neglecting energy recovery in the discharging phase

$$\text{SEC} = \frac{IV_{\text{ext}}T + \mathcal{V}\Delta p/\eta_{\text{pump}}}{\mathcal{V}} = FV_{\text{ext}}\Delta c + \frac{\Delta p}{\eta_{\text{pump}}}, \tag{F.11}$$

where the current $I = A\langle j\rangle F$ and we used Eq. (F.9) with $\Delta c = \text{SR} \times c_0$ the average removed salt concentration.

#### F.5.2. Energy normalized adsorbed salt (ENAS)

A derived secondary metric is the *energy-normalized adsorbed salt* [mol/J]

$$\text{ENAS} = \frac{\Delta c}{\text{SEC}} = \frac{\Delta c}{FV_{\text{ext}}\Delta c + \frac{\Delta p}{\eta_{\text{pump}}}}. \tag{F.12}$$

This metric combines the need for both increasing the average desalinated concentration difference $\Delta c$ and decreasing the specific energy consumption SEC. Through Eq. (F.9) it simply inversely proportional to the applied voltage when neglecting the pumping energy. It is somewhat reminiscent of an energy efficiency, although in units of mol/J rather than J/J.

Further multiplying with the productivity gives in [mol·m/J·s]

$$\text{PENAS} = \frac{\text{P}\Delta c}{\text{SEC}} = \frac{\frac{L_s}{L}U\Delta c}{FV_{\text{ext}}\Delta c + \frac{\Delta p}{\eta_{\text{pump}}}}. \tag{F.13}$$

This metric shows the need to both minimize the energy used per amount water treated and increase the productivity. As such it may be a useful quantity to maximized, or its inverse can be treated as a cost function to be minimized. With ASAR=P$\Delta c$ the relation between the various metrics given here was also given in e.g. Ref. [24]. A similar metric, dubbed the energetic operational metric, EOM = ASAR × ENAS = P$(\Delta c)^2$/SEC was proposed in Ref. [26].

#### F.5.3. Power efficiency

We may alternatively introduce an energy efficiency based on what energy has to be spent under equilibrium conditions compared to what is actually spent. Here we assume that, of the various components making up $V_{\text{ext}}$ in Eq. (6), the Donnan and micropore potential drops are unavoidable, while the ohmic drop can be avoided by approaching equilibrium. Including also dissipation in the pump gives

$$\eta_{\text{power}} \equiv \frac{2I(\Delta\phi_{\text{D}} + \Delta\phi_{\text{m}})}{IV_{\text{ext}} + \mathscr{V}\Delta p/T\eta_{\text{pump}}} = \frac{1}{1 + \frac{\Delta\phi_\Omega + P\Delta p/2F\eta_{\text{pump}}j}{\Delta\phi_{\text{D}} + \Delta\phi_{\text{m}}}}. \tag{F.14}$$

#### F.5.4. Thermodynamic energy efficiency (TEE)

As argued in Ref. [58] the SEC cannot be used as a measure of energy efficiency since it does not take into account how difficult a separation is by involving the Gibbs free energy of separation [6].

The Thermodynamic energy efficiency is defined as TEE = $\Delta G$/SEC. Somewhat resembling the ENAS it is an actual energy efficiency between 0 and 1.

## Appendix G. Comparison with Ref. [37]

In our notation the dimensionless equations formulated in Ref. [37] read:

$$\frac{\partial \bar{c}}{\partial \check{x}} = \bar{C} - \bar{c}, \tag{G.1}$$

$$\frac{\partial \bar{C}}{\partial \check{t}} = \bar{c} - \bar{C}, \tag{G.2}$$

where $\bar{C} = C/c_0$ with $C$ the salt concentration in the electrode per total unit volume, not just of the liquid, is assumed to be independent of $y$. The solution can be expressed as a series expansion:

$$\bar{c}(x,t) = \bar{C}_0 + \left(1-\bar{C}_0\right)\mathrm{e}^{-\check{x}-\check{t}}\sum_{m=0}^{\infty}\frac{\check{t}^m}{m!}\sum_{j=0}^{m}\frac{\check{x}^j}{j!}, \tag{G.3}$$

where[34]

$$\bar{C}_0 = \frac{L_\mathrm{s}/L_\mathrm{e}}{1+\Delta\bar{\phi}_{\Omega,s}/2}, \tag{G.4}$$

$$\check{x} = \frac{2Dx}{UL_\mathrm{s}^2}\left(1+\Delta\bar{\phi}_{\Omega,s}/2\right), \tag{G.5}$$

$$\check{t} = \frac{2D}{L_\mathrm{e}L_\mathrm{s}}\left(t-x/U\right). \tag{G.6}$$

here $\Delta\bar{\phi}_{\Omega,s} = \Delta\phi_{\Omega,s}/V_T$ with $\Delta\phi_{\Omega,s}$ the ohmic potential drop over the spacer width driving the ionic current. Here $1+\Delta\bar{\phi}_{\Omega,s}/2$ represents the enhancement of diffusion, by migration.

There is a superficial similarity between Eqs. (G.1)-(G.2) and Eqs. (52)-(53). The electrode concentration $C$ is assumed to increase from an initial value $C_0$ allowing the channel concentration to decrease as long as $c > C$. Equation number two of Ref. [37] shows that, moving along with the flow, any decrease in $c$ increases $C$ until $C = c$. Adding Eqs. (G.1) and (G.2) gives $\frac{\partial C}{\partial t} + \frac{\partial \bar{c}}{\partial \tilde{x}} = 0$, similar to $\frac{\partial \tilde{\zeta}}{\partial \tilde{t}} + \frac{\partial \bar{c}}{\partial \tilde{x}} = 0$ obtained by adding Eqs. (52)-(53). This shows conservation of concentration. However, while in our case salt is adsorbed. In Ref. [37] the salt merely moves from the spacer into the electrode, increasing the local concentration there. This could be representative of the final phase where the electrode adsorption capacity is fully reached. Additionally, in our model we include a transport resistance inside the electrode which increases with time as more of the adsorption capacity saturates. Therefore, the capacitance of the electrode plays a role in our time-scale $\tilde{t}$ while it does not appear in $\hat{t}$.

## Appendix H. Initial phase

During the first transit time $0 < t < t_U$ several things happen at the same time resulting in a hard-to predict outlet concentration. A crude but mathematically simple approximation is, despite that this is clearly not valid, to consider the spacer as a perfectly mixed domain and write for the difference between inlet and outlet concentration [3,29][35]

$$c_0 - c_\mathrm{out}^t = \frac{\langle j\rangle L}{UL_\mathrm{s}}\left(1-\mathrm{e}^{-\frac{t}{t_U}}\right), \tag{H.1}$$

where the superscript $t$ is used to indicate that $c_\mathrm{out}^t$ is an approximation for all time, so also $t < t_U$. For longer times it reduces to Eq. (F.8). This result was slightly generalized in Refs. [24,51] to consider the case in which the initial concentration is not at the inlet concentration but at $c_{(0)}$, adding a term $\left(c_0 - c_{(0)}\right)\mathrm{e}^{-t/t_U}$ to Eq. (H.1).

Eq. (H.1) shows that for equal $\langle j\rangle L/UL_\mathrm{s}$ the concentration profiles as a function of $t/t_U$ will be the same, referred to as self-similarity in Ref. [51]. Our reduction to just the variables $\tilde{t}$ and $\tilde{x}$ show a similar data-collapse or "collapse to a curve" but for longer times $t \gtrsim t_U$ under diffusion-limited conditions.

Inserting Eq. (F.8)

$$\bar{c}_\mathrm{out}^t = 1 - \min\left(1, \frac{\tilde{L}}{\sqrt{1+2\tilde{t}}}\right)\left(1-\mathrm{e}^{-\frac{t}{t_U}}\right). \tag{H.2}$$

Eq. (H.2) gives $\bar{c}_\mathrm{out} = 1$ for $t = 0$, while it tends to Eq. (68) in case $t \gg t_U$. Therefore, this approach may also be seen as a pragmatic way of modifying the analytical solutions in such a way that they satisfy also the actual initial condition $c = 1$.

## Appendix I. Computational model

Some numerical stability issues were encountered, primarily due to the sharp transition to zero salt concentration inside the electrodes. We implemented similar stabilisation methods as proposed in Ref. [41], but further included a transformation to exponential concentration to ensure non-negativity and reduce variable scaling difference in the shocks. The computational model was formulated following the description laid out in Eqs. (9)-(17) in Ref. [27]. Due to the symmetries of the system only the half $y > 0$ of the electrode-spacer configuration was modelled. The equations were

[34] Taking for the effective specific conductance "$\tau\Lambda$" in Ref. [37] the dilute result $\frac{\kappa_{c,0}}{2c_0} = \frac{F^2D}{RT} = \frac{FD}{V_T}$ we obtain for the coefficients $k_1 = \frac{2D\left(1+\Delta\bar{\phi}_{\Omega,s}/2\right)}{L_s^2}$ and $k_2 = \frac{2D}{L_eL_s}$ and $\bar{C}_0 = \frac{L_e}{L_s}\frac{k_2}{k_1}$.

[35] Here $E = \mathrm{e}^{-\frac{t}{t_U}}$ is the (normalized) exit-age or residence-time distribution (RTD) of an ideally mixed reactor. In reality the spacer region may be far from well-mixed so that instead we may replace the exponent with a more suitable RTD or E-function. For example, an ideal plug flow reactor with residence time $t_U$ in series with a CSTR with residence time $t_\mathrm{CSTR}$ has $E = \mathrm{e}^{-\frac{t-t_U}{t_\mathrm{CSTR}}}$. In case the spacer region is empty it may be approximately described by a fully-developed planar Poiseuille flow. A planar laminar flow-reactor without axial dispersion has $E = 0$ for $t < 2t_U/3$ as nothing of the inlet reaches the outlet before 2/3 of the average residence time and $E = \frac{1}{3(t/t_U)^3\sqrt{1-t_U/3t}}$ for $t > 2t_U/3$ [34] so that $\int E dt = 1$. Taylor-Aris dispersion due to laminar mixing may be added to this. If instead of an empty space the spacer region contains a spacer material that is more like a porous medium the RTD may become closer to that of a plug-flow reactor.

solved using equation based interfaces in COMSOL Multiphysics, in which the concentration variable was substituted with an exponential term, i.e.

$$C = e^{c} \quad \text{or} \quad c = \log C, \tag{I.1}$$

which entirely precludes erroneous negative concentrations and obviates the need for variable rescaling, together allowing for faster computation at greater potentials.

## Appendix J. Supplementary data

Supplementary data to this article can be found online at https://doi.org/10.1016/j.desal.2024.117408.

## References


[1] Mohammad A. Alkhadra, Su Xiao, Matthew E. Suss, Huanhuan Tian, Eric N. Guyes, Amit N. Shocron, Kameron M. Conforti, J. Pedro, Nayeong de Souza, Michele Tedesco Kim, et al., Electrochemical methods for water purification, ion separations, and energy conversion, Chem. Rev. 122 (16) (2022) 13547–13635.

[2] M. Andelman, The flow through capacitor: a new tool in wastewater purification, Filtration & Separation 35 (4) (1998) 345–348.

[3] Marc Andelman, Flow through capacitor basics, Sep. Purif. Technol. 80 (2) (2011) 262–269.

[4] Eran Avraham, Yaniv Bouhadana, Abraham Soffer, Doron Aurbach, Limitation of charge efficiency in capacitive deionization: I. on the behavior of single activated carbon, J. Electrochem. Soc. 156(6):P95 (2009).

[5] Eran Avraham, Malachi Noked, Izaak Cohen, Abraham Soffer, Doron Aurbach, The dependence of the desalination performance in capacitive deionization processes on the electrodes pzc, J. Electrochem. Soc. 158 (12) (2011) P168.

[6] P.M. Biesheuvel, Thermodynamic cycle analysis for capacitive deionization, J. Colloid Interface Sci. 332 (1) (2009) 258–264.

[7] PM Biesheuvel. Activated carbon is an electron-conducting amphoteric ion adsorbent. *arXiv preprint arXiv:1509.06354*, 2015.

[8] P.M. Biesheuvel, M.Z. Bazant, Nonlinear dynamics of capacitive charging and desalination by porous electrodes, Phys. Rev. E 81 (3) (2010) 031502.

[9] P.M. Biesheuvel, Fu Yeqing, Martin Z. Bazant, Diffuse charge and faradaic reactions in porous electrodes, Phys. Rev. E 83 (6) (2011) 061507.

[10] P.M. Biesheuvel, S. Porada, M. Levi, Martin Z. Bazant, Attractive forces in microporous carbon electrodes for capacitive deionization, J. Solid State Electrochem. 18 (5) (2014) 1365–1376.

[11] P.M. Biesheuvel, A. Van der Wal, Membrane capacitive deionization, J. Membr. Sci. 346 (2) (2010) 256–262.

[12] P.M. Biesheuvel, B. Van Limpt, A. Van der Wal, Dynamic adsorption/desorption process model for capacitive deionization, J. Phys. Chem. C 113 (14) (2009) 5636–5640.

[13] P.M. Biesheuvel, R. Zhao, S. Porada, A. Van der Wal, Theory of membrane capacitive deionization including the effect of the electrode pore space, J. Colloid Interface Sci. 360 (1) (2011) 239–248.

[14] John W. Blair, George W. Murphy, Electrochemical demineralization of water with porous electrodes of large surface area, in: Saline Water Conversion, Advances in Chemistry, ACS Publications, Washington, DC, 1960.

[15] Meile Chu, Weijun Tian, Jing Zhao, Mengyuan Zou, Lu Zhiyang, Dantong Zhang, Junfeng Jiang, A comprehensive review of capacitive deionization technology with biochar-based electrodes: biochar-based electrode preparation, deionization mechanism and applications, Chemosphere 307 (Part 3) (2022) 136024 (19 pages).

[16] Hemant W. Dandekar, Jan A. Puszynski, Vladimir Hlavacek, Two-dimensional numerical study of cross-flow filtration combustion, AICHE J. 36 (11) (1990) 1649–1660.

[17] E. Victoria Dydek, Martin Z. Bazant, Nonlinear dynamics of ion concentration polarization in porous media: the leaky membrane model, AICHE J. 59 (9) (2013) 3539–3555.

[18] Joseph C. Farmer, David V. Fix, Gregory V. Mack, Richard W. Pekala, John F. Poco, The Use of Capacitive Deionization With Carbon Aerogel Electrodes to Remove Inorganic Contaminants From Water, Technical Report, Lawrence Livermore National Lab, 1995.

[19] S. Fransen, J. Fransaer, S. Kuhn, Current and concentration distributions in electrochemical microreactors: numerical calculations and asymptotic approximations for self-supported paired synthesis, Electrochim. Acta 292 (2018) 914–934.

[20] J.G. Gamaethiralalage, K. Singh, S. Sahin, J. Yoon, M. Elimelech, M.E. Suss, P. Liang, P.M. Biesheuvel, R. Linzmeyer Zornitta, L.C.P.M. De Smet, Recent advances in ion selectivity with capacitive deionization, Energy Environ. Sci. 14 (3) (2021) 1095–1120.

[21] Michael Gordon, Galen Suppes, Convection battery—modeling, insight, and review, AICHE J. 59 (8) (2013) 2833–2842.

[22] Eric N. Guyes, Amit N. Shocron, P.M. Anastasia Simanovski, Biesheuvel, and Matthew E Suss., A one-dimensional model for water desalination by flow-through electrode capacitive deionization, Desalination 415 (2017) 8–13.

[23] H. Hassanzadeh, J. Abedi, M. Pooladi-Darvish, Accurate numerical simulation of reaction front propagation, in: Canadian International Petroleum Conference, OnePetro, 2008.

[24] Steven A. Hawks, Jennifer M. Knipe, Patrick G. Campbell, Colin K. Loeb, McKenzie A. Hubert, Juan G. Santiago, Michael Stadermann, Quantifying the flow efficiency in constant-current capacitive deionization, Water Res. 129 (2018) 327–336.

[25] Steven A. Hawks, Ashwin Ramachandran, Slawomir Porada, Patrick G. Campbell, Matthew E. Suss, P.M. Biesheuvel, Juan G. Santiago, Michael Stadermann, Performance metrics for the objective assessment of capacitive deionization systems, Water Res. 152 (2019) 126–137.

[26] Ali Hemmatifar, James W. Palko, Michael Stadermann, Juan G. Santiago, Energy breakdown in capacitive deionization, Water Res. 104 (2016) 303–311.

[27] Ali Hemmatifar, Michael Stadermann, Juan G. Santiago, Two-dimensional porous electrode model for capacitive deionization, J. Phys. Chem. C 119 (44) (2015) 24681–24694.

[28] Jingsong Huang, Rui Qiao, Guang Feng, Bobby G Sumpter, and Vincent Meunier. Modern Theories of Carbon-based Electrochemical Capacitors, 2013.

[29] YAC Jande and Woo-Seung Kim, Desalination using capacitive deionization at constant current, Desalination 329 (2013) 29–34.

[30] Allan M. Johnson, A. Wayne Venolia, G. Wilbourne Robert, John Newman, The Electrosorb Process for Desalting Water, Technical report, US Department of Interior, 1970.

[31] AM Johnson and John Newman, Desalting by means of porous carbon electrodes, J. Electrochem. Soc. 118 (3) (1971) 510.

[32] William Morrow Kays, Michael E Crawford, and Bernhard Weigand. Convective Heat and Mass Transfer, volume 3. McGraw-Hill New York, 1993.

[33] T. Kim, J.E. Dykstra, S. Porada, A. Van Der Wal, J. Yoon, P.M. Biesheuvel, Enhanced charge efficiency and reduced energy use in capacitive deionization by increasing the discharge voltage, J. Colloid Interface Sci. 446 (2015) 317–326.

[34] Octave Levenspiel, Chemical Reactor Omnibook, Oregon State University Bookstores Inc., Corvallis Oregon, 1989.

[35] Ali Mani, Martin Z. Bazant, Deionization shocks in microstructures, Phys. Rev. E 84 (6) (2011) 061504.

[36] T.M. Mubita, J.E. Dykstra, P.M. Biesheuvel, A. Van Der Wal, S. Porada, Selective adsorption of nitrate over chloride in microporous carbons, Water Res. 164 (2019) 114885.

[37] G.W. Murphy, D.D. Caudle, Mathematical theory of electrochemical demineralization in flowing systems, Electrochim. Acta 12 (12) (1967) 1655–1664.

[38] Heena K. Mutha, H. Jeremy Cho, Mazdak Hashempour, Brian L. Wardle, Carl V. Thompson, Evelyn N. Wang, Salt rejection in flow-between capacitive deionization devices, Desalination 437 (2018) 154–163.

[39] D.A. Nield, Forced convection in a parallel plate channel with asymmetric heating, Int. J. Heat Mass Transf. 47 (25) (2004) 5609–5612.

[40] J. Nordstrand, D. Joydeep, Relaxed adsorption-flow coupling enables stable comsol multiphysics modeling of upscaled capacitive deionization, in: COMSOL Conference 2020, COMSOL Grenoble, Grenoble, 2020.

[41] Johan Nordstrand, Joydeep Dutta, A new automated model brings stability to finite-element simulations of capacitive deionization, Nano Select 3 (6) (2022) 1021–1035.

[42] Y. Oren, A. Soffer, Electrochemical parametric pumping, J. Electrochem. Soc. 125 (6) (1978) 869.

[43] Yoram Oren, Capacitive deionization (cdi) for desalination and water treatment—past, present and future (a review), Desalination 228 (1–3) (2008) 10–29.

[44] Valeria Palomba, Andrea Frazzica, Modeling of sorption systems for thermal energy storage, in: Advances in Thermal Energy Storage Systems, Elsevier, 2021, pp. 453–475.

[45] Shu-Yuan Pan, Seth W. Snyder, Hwong-Wen Ma, Yupo J. Lin, Pen-Chi Chiang, Development of a resin wafer electrodeionization process for impaired water desalination with high energy efficiency and productivity, ACS Sustain. Chem. Eng. 5 (4) (2017) 2942–2948.

[46] Sohum K. Patel, Cody L. Ritt, Akshay Deshmukh, Zhangxin Wang, Mohan Qin, Razi Epsztein, Menachem Elimelech, The relative insignificance of advanced materials in enhancing the energy efficiency of desalination technologies, Energy Environ. Sci. 13 (6) (2020) 1694–1710.

[47] S. Porada, M. Bryjak, A. Van Der Wal, P.M. Biesheuvel, Effect of electrode thickness variation on operation of capacitive deionization, Electrochim. Acta 75 (2012) 148–156.

[48] S. Porada, L. Weinstein, R. Dash, A. Van Der Wal, M. Bryjak, Y. Gogotsi, P. M. Biesheuvel, Water desalination using capacitive deionization with microporous carbon electrodes, ACS Appl. Mater. Interfaces 4 (3) (2012) 1194–1199.

[49] S. Porada, R. Zhao, A. Van Der Wal, Volker Presser, P.M. Biesheuvel, Review on the science and technology of water desalination by capacitive deionization, Prog. Mater. Sci. 58 (8) (2013) 1388–1442.
[50] Mohan Qin, Akshay Deshmukh, Razi Epsztein, Sohum K. Patel, Oluwaseye M. Owoseni, W. Shane Walker, Menachem Elimelech, Comparison of energy consumption in desalination by capacitive deionization and reverse osmosis, Desalination 455 (2019) 100–114.
[51] Ashwin Ramachandran, Ali Hemmatifar, Steven A. Hawks, Michael Stadermann, Juan G. Santiago, Self similarities in desalination dynamics and performance using capacitive deionization, Water Res. 140 (2018) 323–334.
[52] Yasamin Salamat, Carlos H. Hidrovo, A parametric study of multiscale transport phenomena and performance characteristics of capacitive deionization systems, Desalination 438 (2018) 24–36.
[53] Yong-Uk Shin, Jihun Lim, Chanhee Boo, Seungkwan Hong, Improving the feasibility and applicability of flow-electrode capacitive deionization (fcdi): review of process optimization and energy efficiency, Desalination 502 (2021) 114930.
[54] A.N. Shocron, M.E. Suss, Should we pose a closure problem for capacitive charging of porous electrodes? EPL (Europhysics Letters) 130 (3) (2020) 34003.
[55] Matthew E. Suss, Theodore F. Baumann, William L. Bourcier, Christopher M. Spadaccini, Klint A. Rose, Juan G. Santiago, Michael Stadermann, Capacitive desalination with flow-through electrodes, Energy Environ. Sci. 5 (11) (2012) 9511–9519.
[56] M.E. Suss, Slawomir Porada, P.M. Xiaowei Sun, Jeyong Yoon Biesheuvel, Volker Presser, Water desalination via capacitive deionization: what is it and what can we expect from it? Energy Environ. Sci. 8 (8) (2015) 2296–2319.
[57] Wangwang Tang, Jie Liang, Di He, Jilai Gong, Lin Tang, Zhifeng Liu, Dongbo Wang, Guangming Zeng, Various cell architectures of capacitive deionization: recent advances and future trends, Water Res. 150 (2019) 225–251.
[58] J.E. Li Wang, Dykstra, and Shihong Lin., Energy efficiency of capacitive deionization, Environ. Sci. Technol. 53 (7) (2019) 3366–3378.
[59] Wu Peng, Jingsong Huang, Vincent Meunier, Bobby G. Sumpter, Rui Qiao, Voltage dependent charge storage modes and capacity in subnanometer pores, The Journal of Physical Chemistry Letters 3 (13) (2012) 1732–1737.
[60] Wu Weixiong, Shiwei Xie, Wencan Zhang, Ruixin Ma, Junjie Yang, Zhonghao Rao, Role of natural convection and battery arrangement for phase change material based battery thermal management unit, Journal of Energy Storage 52 (2022) 104820.
[61] Fan Yang, Yunfei He, Leon Rosentsvit, Matthew E. Suss, Xiaori Zhang, Tie Gao, Peng Liang, Flow-electrode capacitive deionization: a review and new perspectives, Water Res. 200 (2021) 117222.
[62] Changyong Zhang, Jinxing Ma, Wu Lei, Jingyi Sun, Li Wang, Tianyu Li, T. David, Waite., Flow electrode capacitive deionization (fcdi): recent developments, environmental applications, and future perspectives, Environ. Sci. Technol. 55 (8) (2021) 4243–4267.
[63] Xudong Zhang, Kuichang Zuo, Xiaori Zhang, Changyong Zhang, Peng Liang, Selective ion separation by capacitive deionization (cdi) based technologies: a state-of-the-art review, Environ. Sci.: Water Res. Technol. 6 (2) (2020) 243–257.
[64] R. Zhao, P.M. Biesheuvel, H. Miedema, H. Bruning, A. Van der Wal, Charge efficiency: a functional tool to probe the double-layer structure inside of porous electrodes and application in the modeling of capacitive deionization, The Journal of Physical Chemistry Letters 1 (1) (2010) 205–210.
[65] R. Zhao, P.M. Biesheuvel, A. Van der Wal, Energy consumption and constant current operation in membrane capacitive deionization, Energy Environ. Sci. 5 (11) (2012) 9520–9527.
[66] R. Zhao, S. Porada, P.M. Biesheuvel, A. Van der Wal, Energy consumption in membrane capacitive deionization for different water recoveries and flow rates, and comparison with reverse osmosis, Desalination 330 (2013) 35–41.
[67] R. Zhao, O. Satpradit, H.H.M. Rijnaarts, P.M. Biesheuvel, A. Van der Wal, Optimization of salt adsorption rate in membrane capacitive deionization, Water Res. 47 (5) (2013) 1941–1952.
[68] Xing Zhou, Guan Huei See, Guojun Zhu, Shihuan Lin, Chengqing Wei, Junbin Zhang, Unified regional modeling approach to emerging multiple-gate/nanowire mosfets, in: 2008 9th International Conference on Solid-state and Integrated-circuit Technology, IEEE, 2008, pp. 262–267.